Atomic scale transformation of bone in controlled aqueous alteration experiments

Julie Aufort, Christel Gervais, Loïc Segalen, Nathalie Labourdette, Cristina Coelho-Diogo, Benoit Baptiste, Olivier Beyssac, Romain Amiot, Christophe Lécuyer, Etienne Balan

Atomic scale transformation of bone in controlled aqueous alteration experiments

Julie Aufort[1], Christel Gervais[2], Loïc Ségalen[3], Nathalie Labourdette[3], Cristina Coelho-Diogo[4], Benoît Baptiste[1], Olivier Beyssac[1], Romain Amiot[5], Christophe Lécuyer[5,6], Etienne Balan[1]

[1]Sorbonne Université, CNRS, IRD, MNHN, Institut de Minéralogie, de Physique des Matériaux et de Cosmochimie, IMPMC, UMR 7590, F-75005, Paris, France

[2]Sorbonne Université, Collège de France, Laboratoire de Chimie de la Matière Condensée de Paris, LCMCP, UMR 7574, F-75005, Paris, France

[3]Sorbonne Université, CNRS-INSU, Institut des Sciences de la Terre de Paris, ISTEP, UMR 7193, F-75005, Paris, France

[4]Sorbonne Université, Institut des Matériaux de Paris Centre, IMPC, FR2482, F-75005, Paris, France

[5]Université Lyon 1, ENS Lyon, CNRS UMR 5276, 2 rue Raphaël Dubois, 69622 Villeurbanne, France

[6]Institut Universitaire de France, 103 boulevard Saint-Michel, 75005 Paris, France

Corresponding author: Julie Aufort, IMPMC, case 115, 4 place Jussieu, 75252 Paris, cedex 05 France
E-mail : Julie.Aufort@upmc.fr Phone: 00.33.1.44.27.42.27 Fax: 00.33.1.44.27.37.85

Abstract

The chemical and isotopic compositions of biogenic apatite are important geochemical markers, which can suffer modifications during fossilisation. Compared with modern ones, fossil apatites generally exhibit variations in carbonate content, enrichment in fluorine, incorporation of trace elements and an increase in crystallinity parameters. Detailed understanding of these transformations induced by fossilisation should help assess the preservation of geochemical records in apatites. In this contribution, we investigate the transformation of modern bone altered under controlled conditions. Modern bone samples were soaked in aqueous solutions of neutral to alkaline pH (9-10) for one and three weeks at various temperatures (20 and 70 °C) and experiments were duplicated in fluorine-free and in 10^{-2} M NaF solutions. Bone transformation was monitored through the modifications of chemical (F, Ca, P) and isotopic ($\delta^{13}C$, $\delta^{18}O_c$, $\delta^{18}O_p$) composition as well as using vibrational (ATR-FTIR, Raman) and solid-state (^1H, ^{13}C, ^{19}F) NMR spectroscopies. The observed modifications sustain a transformation mechanism through partial dissolution of biogenic apatite and precipitation of secondary apatite. This transformation occurs irrespective of the presence or absence of fluorine and leads to the formation of carbonate-bearing fluorapatite or carbonate-bearing hydroxylapatite, respectively. The fraction of secondary apatite seems to be limited to ~60 %, suggesting that its

formation has a protecting role against further dissolution of the primary apatite. The observation of clumped (CO_3^{2-}, F^-) defect in the structural B-site of some samples as well as perturbation of the isotopic compositions attest to carbonate incorporation in the secondary apatite. Although the incorporation of fluoride ions can serve as a probe revealing dissolution-recrystallisation of bone, the present study also underlines the difficulty to systematically relate mineralogical transformations to an open-system behaviour in bioapatite.

1. Introduction

Bones and teeth are composed of three constituents: a mineral component and a fraction of organic and water molecules (Pasteris et al., 2008). The mineral component is a form of hydroxyl-deficient nanocrystalline carbonate-bearing hydroxylapatite ($Ca_5(PO_4)_3(OH)$) (Elliott, 2002). During biomineralisation, the stable isotope compositions of structural carbonate and phosphate groups in bioapatite record a combination of environmental features and biological processes. Carbon and oxygen isotope ratios (expressed as $\delta^{13}C$ and $\delta^{18}O$ values) in bioapatite reflect that of ingested food (DeNiro and Epstein, 1978; Lee-Thorp et al., 1989; Cerling and Harris, 1999; Passey et al., 2005) and drinking water (Longinelli, 1984). They can provide information on the dietary preferences (Cerling et al., 1999) of vertebrates and on the climatic conditions that prevailed in the environment (Fricke et al., 1998; Levin et al., 2006). The stable isotope compositions of fossil remains of vertebrates are thus widely used to reconstruct past climates and past environments (e.g. Kohn and Cerling, 2002; Amiot et al., 2004; Kingston and Harrison, 2007; Tütken et al., 2008; Roche et al., 2013).

The fossilisation process involves several mechanisms that can affect the mineralogical and crystal-chemical composition of vertebrate skeletal tissues: degradation of the organic matrix, variation of the carbonate content, diagenetic enrichment of exogenous trace elements such as rare earth elements and fluorine, as well as an increase in crystallinity (e.g. Hedges, 2002; Trueman et al., 2008; Roche et al., 2010; Reynard and Balter, 2014; Keenan et al., 2015). However not all skeletal tissues exhibit the same chemical-structural characteristics. Bones consist of about 50 vol% of ~ 2 nm thick, 10-20 nm wide and 20-50 nm long apatitic nanocrystallites and a nearly equivalent volume of collagen fibrils (Glimcher, 2006; Pasteris et al., 2008). In contrast, tooth enamel is made of ~90 vol% of larger apatite crystallites and low organic matter and water content (LeGeros and LeGeros, 1984, Elliott, 2002). In bones, the smaller crystal size leads to a high specific surface area, resulting in higher reactivity and solubility compared to tooth enamel (LeGeros, 1991, Berna et al., 2004). Bone is thus expected

to be less resistant to post-mortem alteration than the more mineralised and less porous tooth enamel (Michel et al., 1995; Lee-Thorp and Sponheimer, 2003; Pasteris and Ding, 2009). For this reason, palaeoenvironmental reconstructions in continental environments are mainly carried out based on stable isotope analysis of fossil enamel (Wang and Cerling, 1994; Ayliffe et al., 1994). However, fossil enamel may be scarce in certain fossilisation contexts whereas bone fossils can be retrieved in larger quantities and a few major taxa do not have any teeth, such as most birds, turtles or primitive fish. Moreover, while enamel is mineralised during childhood in mammals, bone apatite also provides dietary information about adult life stages that can be further completed by the joint stable isotope analysis of collagen, when preserved (Lee-Thorp and Sponheimer, 2003; Lee-Thorp, 2008). Furthermore, the study of bone diagenetic processes has wide implications, e.g. in archaeological contexts where preservation assessment of bones is key to bone collagen dating (Lebon et al., 2016) and in oceanic environments where biomineralised tissues of Devonian fish shed light on their ontogeny and taphonomy (Chevrinais et al., 2015).

Overall, fossil bones and teeth often display a transformation of the original apatite towards a carbonated fluorapatite. This transformation can be understood in the light of the more general processes of mineral replacement reactions through dissolution-recrystallisation at the solid/solution interface (Putnis, 2002; Putnis and Putnis, 2007; Wang et al., 2013). It most likely occurs via a dissolution/recrystallization mechanism driven by the lower solubility of fluorapatite (Kolodny, 1996; Trueman and Tuross, 2002). Recent study of early diagenetic processes suggested that formation of fluorine-enriched apatite can occur rapidly, within one month of burial (Keenan and Engel, 2017). Studies that have focused on the incorporation of rare earth and trace elements in fossil bone also suggest that diffusion processes pervasively affect the organo-mineral composite (Millard and Hedges, 1996, Kohn, 2008). Accordingly, the extent of diagenetic transformations can be assessed from the chemical or isotopic composition characteristics of fossils, whereas optical or scanning electron microscopic observations may fail to detect incipient transformations of apatite.

Mineralogical investigations based on vibrational FTIR or Raman spectra, and X-ray diffraction (XRD) can also bring precious information on the transformations of biomaterials. They often rest on the estimation of crystallinity indices (Shemesh, 1990, Weiner and Bar-Yosef, 1990, Person et al. 1995, Sillen and Morris, 1996, Sponheimer and Lee-Thorp, 1999), accounting for modifications of the size and/or structural order of apatite particles. These indices are technique-dependent and can differently reflect the natural heterogeneity of

bioapatites (Surovell and Stiner, 2001; Nakano et al., 2002). As a result, explicit correlations are hardly identified between crystallinity indices and intake in trace elements or perturbation of the isotopic composition of fossils (Pucéat et al., 2004; Trueman et al., 2008).

These previous studies call for in-depth analysis of the atomic scale transformations of bone when exposed to aqueous fluids. In the present contribution, artificial alteration experiments are carried out on modern bone samples in order to better specify the physico-chemical mechanisms involved in bone diagenesis. Modifications of the chemical and stable isotope ($\delta^{13}C$, $\delta^{18}O$) compositions observed on the reacted samples are interpreted under the light of the crystal-chemical transformations inferred from their vibrational spectra (ATR-FTIR, Raman), solid-state Nuclear Magnetic Resonance (^{19}F, ^{13}C, and ^{1}H NMR) spectra and X-ray diffraction (XRD) patterns. A special attention is given to the role of fluorine and to the behaviour of structural carbonate groups in the transformation mechanism.

2. Materials and Methods

2.1. Samples description and alteration conditions

The materials used in the following alteration experiments all come from a metapodial bone of modern ox, TH1, collected on the shores of the Bogoria Lake (Kenya). This sample presented the usual characteristics of biological bone and no evidence was found of significant alteration prior to performing the following experiments. Two types of samples were investigated to provide complementary results: bone powders allowed for a high rate of transformation and bone wafers provided spatially resolved information about the alteration process. The cortical bone was sawn into 1 to 2 mm wide and thick, and about 5 mm long wafers using a low-speed IsoMet diamond-edged saw. Bone powders were obtained with a rotary drill equipped with a diamond-tipped burr and ground with an agate mortar and pestle. These bone wafers and powders were used directly in the alteration experiments described below without any pre-treatment. Either the bone wafer or bone powder (~ 600 mg) were soaked in 100 mL of solution prepared from MilliQ water ($\delta^{18}O$ = -6.7 ‰ V-SMOW) for various amounts of time listed in Table 1 without stirring. The solution was then filtered to collect the powder sample while the wafer was retrieved and rinsed with MilliQ water. In both cases, samples were then left to dry overnight in an oven at 60 °C. Various alteration conditions were investigated and are described in Table 1. Following the protocol used for the experimental fluorination of modern horse tooth by Pasteris and Ding (2009), a phosphate buffer solution (Fisher Chemical, Fisher Scientific UK, Loughborough, Leics) was used at pH 7. A phosphate-free 20 mM piperazine-N,N'-bis(2-

ethanesulfonic acid) (PIPES) solution ("organic buffer") was also tested as pH 7 buffer. For alkaline conditions, 100 mL of KOH solutions at pH 9 (10^{-5} M) and pH 10 (10^{-4} M) were used. For each pH condition, alteration experiments were duplicated using either a fluorine-free solution or a fluorinated solution with a 10^{-2} M NaF concentration. Throughout the manuscript, each experiment is referred to by a letter, the prime symbol referring to the fluorinated sample. Reacted samples in fluorine-free solutions will be referred to as control samples. Finally, a natural sample originating from the sedimentary phosphate deposit of Taiba, Senegal, was used as a reference sample for carbonated fluorapatite (C-Fap; Morin et al. 2002).

2.2. Analytical techniques

Fluorine content and Ca/P ratios are reported in Table 2. For each analysis, 100 mg of sample was dissolved in 5 mL of a 30% suprapure nitric acid solution for 1h at 80°C following the protocol previously used by Maurer et al. (2011). Fluorine content was measured using a fluoride ion selective electrode (Mettler Toledo), Ca was measured by energy dispersive X-ray fluorescence (Niton XL3t Thermo Fischer scientific) and phosphorus by spectrophotometry (Milton Roy Spectronic 301 spectrometer). The estimated analytical error based on the analysis of a certified reference material (bone ash SRM 1400) expressed as RSD is 11% for F, 3% for Ca and 4% for P.

ATR-FTIR spectra were recorded using a Quest ATR device and a Nicolet 6700 FTIR spectrometer. A few milligrams of pure powder samples were packed at the surface of the ATR crystal and two different spectra were recorded for each sample, using either a diamond or a Ge ATR crystal, between 400 and 4000 cm^{-1} by averaging 200 scans with a resolution of 1 cm^{-1}. The use of a diamond (n = 2.4) ATR crystal allows the detection of relatively weak bands, such as those ascribed to structural carbonate groups, whereas Ge (n = 4) ATR is less affected by electrostatic effects and provides a better insight into the sample microscopic structure (Aufort et al., 2016; Balan et al., 2019). All ATR spectra are reported in absorbance units A=log(I_0/I_R) where I_0 and I_R are the intensities of the incident and reflected light, respectively. Detailed analysis of the ν_1 PO_4 and ν_2 CO_3 ATR-FTIR bands was performed after a baseline subtraction using the Baseline Spline procedure from Igor Wavemetrics. To evaluate the asymmetry of the ν_1 PO_4 band, the Half Width at Half Maximum on the high frequency side (HWHM) was determined by constructing a vertical line at the position of the peak maximum and measuring the width from that line to the high frequency side of the band at half maximum.

Raman spectra were obtained using a Renishaw InVia Reflex spectrometer. The Raman instrument had been initially calibrated using a standard Neon-Argon lamp and the frequency calibration was checked and corrected daily using a silicon wafer (peak at 520 cm^{-1}). A microscope was used to focus the 532 nm laser beam on a ~ 2-3 µm spot with a x 50 long-working distance objective (numerical aperture 0.45). A maximal 5 mW laser power was delivered at the sample surface, ensuring negligible thermal effects. Detailed analysis of the ν_1 PO$_4$ Raman peak was performed after a baseline subtraction using the Baseline Spline procedure from Igor wavemetrics. Spectral parameters were extracted by fitting with a Voigt function with an uncertainty on peak position and width of ±0.1 cm^{-1} and ±0.5 cm^{-1} respectively.

X-Ray powder diffraction measurements were carried out on a Panalytical Empyrean diffractometer using Cu K$_\alpha$ radiation source ($\lambda_{K\alpha1}$=1.540598Å, $\lambda_{K\alpha2}$=1.544426Å) and a PIXcel3D detector. X-ray data were collected between 5° and 130° 2θ with a 0.01° 2θ step for 7 h. Cell parameters, mean coherent domain (MCD) sizes and microstrain were refined using Le Bail method as implemented in the Fullprof software (Rodriguez-Carvajal, 1993). Starting from the known cell parameters of apatite, the LeBail refinements converged rapidly. Since the peak width was significantly larger than the instrumental resolution (0.05° à *2θ= 50°*), Lorentzian isotropic size (Y) and Lorentzian isotropic strain (X) parameters were refined. The two effects can be decoupled on the diagram measured over a wide angular range because the first induce a peak broadening as Y/cosθ whereas the second as Xtanθ. Then, anisotropic refinements of size parameters significantly improve the fit and the corresponding spherical harmonic coefficients are given in Table S1.

Single-pulse ^{19}F magic angle spinning (MAS) NMR experiments were performed on an Avance 700 Bruker spectrometer (16.3T) operating at 658.93 MHz using a 4 mm rotor at a 14 kHz spinning frequency. Cross-polarization ^{13}C CP MAS NMR experiments were performed on an Avance 300 Bruker spectrometer operating at a Larmor frequency of 75.51 MHz using a 7 mm rotor at a 5 kHz spinning frequency. Single-pulse ^{1}H MAS NMR experiments were performed on an Avance 700 Bruker spectrometer operating at 700.29 MHz using a 2.5 mm rotor at a 30 kHz spinning frequency.

Stable isotope measurements were performed on the carbonate and phosphate components of altered bone powder samples. For the carbonate component, the carbon and oxygen isotope compositions were measured (δ^{13}C, δ^{18}O$_{carbonate}$). Samples weighing 800 µg were analysed on a Kiel IV device coupled to a DeltaVAdvantage IRMS. Samples were reacted under vacuum

with 100% orthophosphoric acid at 70°C to generate water vapour and carbon dioxide. The resultant CO_2 was then purified in an automatic cryogenic trapping system. Measurements were normalised to the NBS 19 standard ($\delta^{13}C = 1.95 \pm 0.02$ ‰ PDB and $\delta^{18}O_c = 28.64 \pm 0.07$ ‰ V-SMOW; n = 3). The stable oxygen isotope ratio of carbonate in bioapatite was calculated using the temperature-dependent fractionation factor between calcite and CO_2 (Kim et al., 2007). Uncertainties given are calculated from measuring the samples three times. Regarding the oxygen isotope composition of the phosphate component ($\delta^{18}O_{phosphate}$), apatite powders were treated following the protocol described by Crowson et al. (1991) slightly modified by Lécuyer et al. (1993). This protocol consists in the isolation of structural phosphate in apatite as silver phosphate (Ag_3PO_4) crystals using acid dissolution and anion-exchange resin. After dissolution of 15 mg of powdered bone in 2 mL of 2 M HF at 25 °C for 24 h, the CaF_2 residue was separated from the solution that contained the phosphate by centrifugation. This solution was then neutralised by adding 2.2 mL of 2 M KOH. Then, 2.5 mL of Amberlite™ anion-exchange resin was added to the solution to separate the PO_4^{3-} ions. The solution was removed after 24 h and the resin was eluted with 27.5 mL of 0.5 M NH_4NO_3 for 4 h. A volume of 0.5 mL of NH_4OH and 15 mL of an ammoniacal solution of $AgNO_3$ were then added and the samples were placed in a thermostated bath at 70°C for 7 h, allowing the precipitation of Ag_3PO_4 crystals. Oxygen isotope compositions were measured using a VarioPYROcube™ elemental analyser (EA) interfaced in continuous flow (CF) mode to an Isoprime™ isotopic ratio mass spectrometer hosted by the Laboratoire de Géologie de Lyon (Université Claude Bernard). For each sample, five aliquots of ~300 µg of silver phosphate were mixed with the same amount of pure graphite powder in silver foil capsules and pyrolysis was performed at 1450 °C. Measurements were calibrated against the NBS120c standard whose value was fixed at 21.7 ‰ (V-SMOW) according to Lécuyer et al. (1993) and the NBS127 (barium sulfate, $BaSO_4$: $\delta^{18}O = 9.3$ ‰ (V-SMOW); Hut, 1987). NBS120c standards that were converted into silver phosphate from each chemistry batch have a mean $\delta^{18}O_p$ value of 21.70 ± 0.51 ‰ (n = 5).

3. Results

3.1. Chemical composition of bone samples

Fluorine content of the unaltered bone TH1 and control samples is about 0.2 wt% (Table 2). Fluorinated bone powders at 70°C contain 2.0 – 2.5 wt.% fluorine whereas the bone powder fluorinated at 20°C (C') contains only 1.6 wt.% fluorine. The Ca/P molar ratio of the unaltered bone is 1.57, consistent with the range of values found in bone (Sillen and LeGeros, 1991, Kourkoumelis et al., 2012) and slightly below the 1.67 value for end-member hydroxylapatite.

All altered bone powders have higher Ca/P molar ratios ranging from 1.64 to 1.86, values typically found in archaeological and fossil bones (Reiche et al., 2003). No significant variation in Ca/P molar ratio is observed from control to fluorinated samples but samples that reacted with phosphate buffered solutions display lower Ca/P ratios than the others.

3.2. Oxygen and carbon isotopic compositions

Oxygen and carbon isotope compositions, i.e. $\delta^{18}O_{carbonate}$, $\delta^{18}O_{phosphate}$, and $\delta^{13}C$, of altered bone powder samples are reported in Table 2. Only minor deviation from the original oxygen isotope composition of structural carbonate in the non-altered bone (36.31 ‰ V-SMOW) is observed in bone powders altered in a phosphate buffer, with $\delta^{18}O_{carbonate}$ values ranging from 35.2 to 37.4 ‰ (V-SMOW). In contrast, bone powders altered in alkaline conditions exhibit lower $\delta^{18}O_{carbonate}$ values, ranging from 32.8 to 34.1 ‰ (V-SMOW). The situation is reversed when considering oxygen phosphate isotope compositions. The $\delta^{18}O_{phosphate}$ of samples altered in a phosphate buffer range between 20.5 and 22.7 ‰. These values are significantly lower than the initial TH1 value (25.8 ‰). Considering that inorganic oxygen exchange of phosphate groups is a very slow process (Lécuyer et al, 1999; Sharp et al., 2000; Zazzo et al., 2004a), this suggests incorporation of phosphate species from the phosphate buffer, which displays a lighter oxygen isotopic composition (12.6 ‰ V-SMOW). Other samples, altered in alkaline conditions and organic buffer, display values ranging from 26.3 to 27.1 ‰ (V-SMOW) close to that of the starting material (25.8‰). Based on isotopic compositions, it is thus possible to distinguish two groups: bone powders altered in a phosphate buffer and bone powders altered in all other conditions. This is most apparent when comparing oxygen isotope composition of phosphate, $\delta^{18}O_{phosphate}$, with carbonate, $\delta^{18}O_{carbonate}$ (Fig 1a). While oxygen isotope compositions of samples altered in alkaline conditions or in the organic buffer fall close to the $\delta^{18}O_{carbonate}$ - $\delta^{18}O_{phosphate}$ correlation line for bioapatites (e.g. Lécuyer et al., 2010), samples altered in the phosphate buffer deviate due to significantly lower $\delta^{18}O_{phosphate}$ values. Importantly, the type of buffer used has more influence on the isotopic composition than the presence or absence of fluoride. Indeed, isotopic compositions do not vary significantly from non-fluorinated samples to their fluorinated counterparts. Regarding carbon isotope compositions (Fig 1b), samples altered in a phosphate buffered condition also show overall ~0.5-0.8 ‰ lower $\delta^{13}C$ values than other samples, regardless of the presence or absence of fluorine.

3.3. X-ray diffraction

XRD patterns show apatite as the only crystalline phase present in altered bone powders (Figure S1). Variations in cell parameters indicate a systematic decrease in the lattice parameter *a* from control to fluorinated bone powders (Table 3). The *a* cell parameter of the original unaltered bone sample TH1 is 9.417 Å. Values of *a* cell parameter in samples fluorinated at 70°C are systematically lower and range between 9.392 and 9.378 Å. An intermediate value is obtained for the sample fluorinated at 20°C (9.403 Å), consistent with its lower fluorine content and closer to that of the original TH1 sample (9.417 Å). The process of soaking bone powders in solution leads to a significant decrease of the strain parameter and all altered samples display smaller mean coherent domain (MCD) sizes in both [020] and [003] directions than the unaltered bone, TH1 (Table 3). Moderately larger MCD sizes are observed in fluorinated samples compared to control samples (Table 3).

3.4. Vibrational spectroscopic study of bone samples

3.4.1. ATR-FTIR spectrum of bone samples

Both diamond and Ge ATR-FTIR spectra of modern bone (Figure 2, Figure S2) display the characteristic absorption bands ascribed to the internal vibrations of apatite phosphate groups, to the structural carbonate incorporated at the A and B sites (hydroxyl and phosphate sites, respectively) of apatite structure and to the amide bands related to the collagen matrix (e.g. Elliott, 2002, Chadefaux et al., 2009). Intense bands observed between 550 and 600 cm^{-1} and between 1010 and 1090 cm^{-1} are related to the ν_4 PO_4 bending and ν_3 PO_4 stretching modes of the structural phosphate groups respectively, while the weaker band at ~960 cm^{-1} is related to the ν_1 PO_4 stretching mode. As previously observed by Aufort et al. (2016), the line shape and particularly the width of the strong ν_4 and ν_3 PO_4 bands is affected by macroscopic electrostatic effects, i.e. related to electrostatic interactions between apatite particles and therefore depending on porosity, grain size and shapes of particles. In contrast, the position and line shape of weaker and narrower bands, such as the ν_1 PO_4 band, are less affected by these electrostatic effects and are thus expected to provide a better insight into the short-range order of the crystal structure (Balan et al., 2011; Aufort et al., 2016, 2018, 2019). However, the overlap of the ν_1 PO_4 band with the stronger ν_3 PO_4 band in the diamond ATR spectrum significantly affects the line shape of the ν_1 PO_4 band. In Ge ATR-FTIR spectra, the overlap between ν_1 and ν_3 PO_4 bands is less pronounced. Information related to the structural order of altered samples was thus extracted from the comparison of ν_1 PO_4 Ge ATR-FTIR bands after baseline subtraction (Figure S3). Note that a systematic decrease in the intensity of amide bands is observed in the ATR-FTIR spectra of all altered bone samples compared to that of unaltered bone. This decrease reflects

the degradation of collagen and is more significant in samples altered in a phosphate buffer at 70°C (D and D') and in the sample fluorinated at pH 9 (F'), for which the amide I band is hardly visible on the ATR-FTIR spectra (Figure S2).

3.4.2. Structural order probed by phosphate vibrational modes in ATR-FTIR and Raman spectra

3.4.2.1. Phosphate stretching bands in ATR-FTIR spectra

The ν_1 PO$_4$ Ge ATR-FTIR band is located at ~960 cm^{-1} in modern ox bone TH1 and at ~966 cm^{-1} in the carbonated fluorapatite (C-Fap) sample. It is well modeled by a large and dominantly Gaussian signal in TH1 while it displays a pronounced Lorentzian shape in C-Fap. The ν_1 PO$_4$ Ge ATR-FTIR band is systematically shifted towards higher frequencies in all bone powder samples altered with fluorine compared to their non-fluorinated counterparts (Figure 3). This shift towards higher vibrational frequencies is consistent with the unit cell volume contraction typically associated with fluoride ion incorporation in the apatite channel sites. All bone powders altered with fluorine at 70°C (D', E', F', G') display a shift of + 2.0 - 2.5 cm^{-1} compared to their respective non-fluorinated counterparts (Table 4). This shift is less pronounced (+ 0.8 cm^{-1}) for the bone powder altered in a phosphate buffer at 20°C (C+NaF). This is consistent with the lower fluorine content (1.6 %) measured in this sample (Table 2) than in bones altered at 70°C (2.0-2.5%). Indeed, the increase in ν_1 PO$_4$ Ge ATR-FTIR frequency correlates with the increase in fluorine content (Figure S4a). In contrast, the Full Width at Half Maximum (FWHM) of the ν_1 PO$_4$ band is not directly correlated with fluoride ion incorporation. Overall, no significant narrowing of the band is observed from non-fluorinated to fluorinated samples (Table 4). The line shape asymmetry was assessed by comparing the Half Width at Half Maximum (HWHM) on the high frequency side of the band to the corresponding full width (FWHM), which is systematically lower in fluorinated samples (Table 4). The asymmetry parameter, defined as $1 - 2(HWHM/FWHM)$ increases with increasing frequency of the ν_1 PO$_4$ band (Figure S4b). The infrared splitting factor (IRSF; Weiner and Bar-Yosef, 1990) determined from the ν_4 PO$_4$ bands on the Ge ATR-FTIR spectra is also broadly correlated to frequency of the ν_1 PO$_4$ band (Figure S5).

3.4.2.2. Phosphate stretching bands in Raman spectra

Complementary information on the fluorine incorporation and structural order of the sample can also be obtained from Raman spectroscopy. An upward shift (+1 cm^{-1}) in the band position of ν_1 PO$_4$ stretch and a decrease (-1 cm^{-1}) in FWHM was observed in the wafer sample altered in NaF for 1 week at 20 °C (Experiment A; Figure 4a). These observations are in agreement

with the results of fluorination experiments carried out by Pasteris and Ding (2009) on dentine under similar conditions and indicate fluorine incorporation in the structure. This is consistent with the similar weaker resistance to alteration of both bone and dentine relative to enamel due to smaller crystallite sizes. No further peak position shift and decrease in FWHM were observed with increased NaF concentration (1 M), as previously observed by Pasteris and Ding (2009), and further fluorination experiments were carried out with 10^{-2} M NaF solutions.

A more pronounced upward shift (+2.5 cm^{-1}) in the ν_1 PO$_4$ band position and decrease (-4 cm^{-1}) in FWHM was observed in the bone powder sample altered with NaF 10^{-2} M for 3 weeks at 20 °C compared to the control sample (Experiment C; Figure 4b). For both samples, Raman spectra were collected on various grains to check the homogeneity, reproducibility and significance of the variations observed in both peak position and FWHM. The longer duration of the experiment and the larger interface between powder and solution can account for the more important variations in Raman spectral features observed in Figure 4b compared to Figure 4a. Spectral parameters, i.e. position of the phosphate peak, FWHM and asymmetry parameter, of the other altered bone powder samples are reported in Table 4.

Concerning the bone wafers soaked in the organic buffer for 3 weeks at 70°C (experiment H), an upward shift (+ 3 cm^{-1}) in the ν_1 PO$_4$ band position and a decrease ($\sim$ - 4 cm^{-1}) in FWHM was observed in the bone wafer altered with NaF 10^{-2} M compared to the control wafer (Figure 4c, Table S2). For both samples, Raman spectra were collected on a transect surface, obtained by cutting perpendicular to the largest face of the wafer to obtain a cross-section in which only the outer edges of the transect have been in direct contact with the solution. Raman spectra were collected at various spots along the transect surface, from the edges to the centre, to provide spatial information on the incorporation of fluorine. Compared to spectra recorded on various grains of the bone powder (Figure S4b), a greater heterogeneity in peak positions and FWHM, ranging 959.7 - 960.6 cm^{-1} and 17.1 - 13.0 cm^{-1} and 962.9 - 963.8 cm^{-1} and 12.5-9.3 cm^{-1} for the control and fluorinated samples respectively, is observed between spectra collected at various spots on the transects. However, no regular trend was observed from the edges to the core of the wafer. The whole transect is thus affected by fluorination, with some spatial variations, suggesting fluoride diffusion through the bulk wafer, i.e. at the millimetre scale.

A decrease in Raman FWHM is systematically observed in samples reacted with fluorinated solutions. Raman spectroscopy thus confirms the results obtained with ν_1 PO$_4$ Ge ATR-FTIR bands and attests of the higher degree of crystalline order in artificially fluorinated samples.

Note that Raman asymmetry parameters are about twice lower than their Ge ATR-FTIR counterparts (Table 4).

3.4.2 Environment of structural carbonate groups inferred from the ν_2 CO_3 band in ATR-FTIR spectra

Regarding structural carbonate groups, diamond ATR-FTIR bands related to the ν_2 out-of-plane bending mode of CO_3^{2-} groups in bone powder samples are observed at 879-881 cm^{-1} for A sites and 871-873 cm^{-1} for B sites (Figure 5a). The broad band centred at ~860-865 cm^{-1}, resulting in a significant asymmetry towards low wavenumbers, is ascribed to labile carbonate groups (Rey et al. 1989; Michel et al. 1995). After normalization of the intensity using the ν_4 PO_4 band, all altered bone samples exhibit a lower carbonate content than the original TH1 sample. Furthermore, the ν_2 CO_3 band intensity decreases from non-fluorinated to fluorinated bone samples. Bone powders altered with fluorine in alkaline conditions (F', G') or at neutral pH in an organic buffer (E') display an additional signal at 865 cm^{-1}. This signal matches that observed in the reference sedimentary carbonated fluorapatite (Figure 5b), i.e. a narrow peak observed at ~865 cm^{-1}. It has been ascribed to a clumped (CO_3^{2-}, F$^-$) defect substituting for the phosphate group in the apatite structure and has also been observed in fossil teeth from the East African Rift (Yi et al. 2013, 2014). In contrast, no signal corresponding to this clumped (CO_3^{2-}, F$^-$) defect is observed in bone powders altered with fluorine in a phosphate buffer (C', D'). The clumped defect signal in the bone powder sample fluorinated in an organic buffer (E') is less intense (by ~2/3) than in bone powders fluorinated in alkaline conditions (F', G'; Figure 5b). Note that there is no significant variation in A/B carbonate ratios between non-fluorinated samples and their fluorinated counterparts, regardless of whether the clumped (CO_3^{2-}, F$^-$) defect is formed or not.

Ge ATR-FTIR spectra of non-fluorinated bone powders, normalised using the ν_4 PO_4 band intensity, are reported in Figure S6a. Although displaying a lower signal/noise ratio, Ge ATR-FTIR spectra of bone powders soaked in a phosphate buffer (C, D, C', D') reveal the presence of a weak and broad signal below the ν_2 CO_3 band on its high frequency side, at ~890 cm^{-1} (Figure S6a and S6b). This spectral feature could not be observed in the matching diamond ATR-FTIR spectra, due to the strong overlap with the electrostatically broadened ν_3 PO_4 band. This signal is accompanied by a decrease in carbonate content compared to the other samples. Apfelbaum et al. (1992) observed a similar spectral feature in FTIR spectra of synthetic carbonated apatites with low carbonate contents and ascribed it to HPO_4^{2-} ions. Indeed, the P-OH stretching mode of HPO_4^{2-} absorbs in the same spectral region as the CO_3 bending mode as

pointed out by Arends and Davidson (1974) who assessed the contribution of HPO_4^{2-} ions to the ν_2 CO_3 signal in healthy and pathologic enamel. Wopenka and Pasteris (2005) also reported on the presence of an additional weak Raman peak around 900 cm^{-1} in calcium phosphate phases containing HPO_4^{2-} ions. The presence of HPO_4^{2-} ions is thus inferred in samples reacted with phosphate buffered solutions.

3.5. Nuclear Magnetic Resonance spectroscopy of bone samples

The ^{13}C CP MAS NMR spectrum of modern bone displays two components related to A-type (~168 ppm) and B-type (~170 ppm) carbonate substitutions, a component at ~173-175 ppm related to the carboxylic acids from amino acids in the organic matrix, as well as numerous signals between 10 and 80 ppm corresponding to organic functions that are enhanced by the Cross-Polarisation sequence (Figure 6a). The ^{13}C CP MAS NMR spectra of bone powders altered in an organic buffer (experiments E, E') and non-fluorinated alkaline solution (F) display a moderate decrease in the signals ascribed to the organic matrix compared to the ^{13}C CP MAS NMR spectrum of unaltered bone. In contrast, spectra of bone powders altered in a phosphate buffer (experiments D, D') and in fluorinated alkaline solution (F') reveal a significant degradation of the organic matrix, which is almost total in the D' sample. Note that the lower signal-to-noise ratio in this sample indicates a less effective cross-polarisation between ^{1}H and ^{13}C nuclei due to a lower amount of protons. Regarding the chemical environment of the carbonate groups, all ^{13}C spectra display predominantly B-type signals at ~170 ppm, which is consistent with the predominant nature of the B-type substitution in bioapatites (Figure 6b).

The ^{19}F MAS NMR spectra of bones altered with fluorine display a main signal at ~ - 102 ppm ascribed to F$^-$ ions incorporated in the channel sites of the apatite structure (Figure 7). This signal is broader in bone samples (FWHM of 6.1 ppm at 20°C and 3.7-4.1 ppm at 70°C) than in the reference sedimentary carbonated fluorapatite (1.8 ppm). A less intense signal is observed in sedimentary carbonated fluorapatite at -88 ppm and corresponds to the clumped (CO_3^{2-}, F^-) defect substituting for the phosphate group in the structure of carbonated fluorapatite (Yi et al. 2013). Due to the low 14 kHz spinning frequency of the rotor in this experiment, the chemical shift anisotropy distributes an important contribution of the fluorine signal into the spinning side bands. For this reason, two spinning side bands are represented on each side of the isotropic signal to better assess the presence or absence of clumped defect in the altered samples. Bone powders altered with fluorine in alkaline conditions (F', G') display the signal at -88 ppm while samples altered in a phosphate buffer (C', D') do not, which is consistent with

the observations made on the ν_2 CO_3 band of diamond ATR-FTIR spectra. ^{19}F NMR spectra of F' and G' suggest that the proportion of fluoride ions incorporated in the channel sites is far greater than that incorporated in the clumped defect, with the area of the clumped defect signal representing about 1% of the total ^{19}F NMR spectrum area in both samples. Unlike the ν_2 CO_3 band, no defect signal could be observed in the sample altered in the organic buffer (E'). As observed in Fig 5, the intensity of the clumped defect in the ν_2 CO_3 diamond ATR-FTIR band is lower for E' than in F' and G'. Furthermore, the broadness and position (-82.2 ppm) of the first spinning side band on the low ppm side may hinder the NMR signal of the clumped defect in E'. The overlap between this spinning side band and a predictably weak clumped defect ^{19}F signal could explain why the latter is not visible in the ^{19}F MAS NMR spectrum of E'.

^{1}H MAS NMR spectra of altered bones display a signal at 0 ppm corresponding to the hydroxyl groups located in the channel sites, aliphatic signals between 1 and 2 ppm associated with the organic matrix of the bone and a large signal at ~5 ppm related to adsorbed water (Figure S7). In the unaltered bone, TH1, channel hydroxyl groups are not observed because of their low concentration (Pasteris et al., 2004; Cho et al., 2013) and significant overlap of their NMR signal with aliphatic signals from the organic matrix. The contribution of aliphatic signals is reduced in artificially altered bone powders, in agreement with the degradation of the organic component observed in their respective ^{13}C NMR spectra. All samples altered with fluorine display a weaker OH channel signal, consistent with an occupation of channel sites by OH^- and F^- ions. A semi quantitative estimation of the fraction of OH^- groups replaced by F^- ions can be obtained by matching the baseline due to the organic component of the control sample and its counterpart altered with fluorine. The OH signal is then fitted by a Gaussian function for the control sample and a Gaussian of identical width and position is used to fit the OH signal of the sample altered with fluorine. In the artificially fluorinated samples, OH channel signals range from 4 to 12 % of that observed in non-fluorinated samples (Table 5). A stoichiometric hydroxylapatite contains about 3.4 wt.% of OH groups but due to a high proportion of vacancies at anionic sites in bones, less than half of OH sites are typically filled with OH groups (Loong et al., 2000), with estimations in the literature ranging from substantial depletion (e.g. 20 % of the expected amount in Cho et al. 2003) to near absence of OH groups (e.g. Pasteris et al., 2004). Even if all channel sites were occupied by OH groups in the control bone samples, percentages of remaining OH groups after fluorination would not exceed 0.4 wt. %. This is consistent with the high fluorine contents measured in the fluorinated samples, ranging between 1.6 and 2.5 wt%. Note that the maximum fluorine amount that can be incorporated in the

channel sites of apatite is 3.8 wt%, therefore not all channel sites are occupied by F^- nor OH^- ions in the fluorinated bone samples investigated here.

4. Discussion

4.1. Evidence of secondary apatite formation

All reacted samples display significant changes of the chemical, isotopic and structural properties of apatite with respect to the original bone. In line with previous observation by Pasteris and Ding (2009), these changes can be interpreted as resulting from the partial dissolution of primary biogenic material and formation of a secondary apatite. In fact, a systematic occurrence of fluoride ions in apatite channel sites of samples reacted with fluorinated solutions is attested by their ^{19}F NMR spectra and can be inferred from the upward shift in ATR-FTIR and Raman v_1 PO_4 band positions and correlated decrease of a cell-parameter (Tables 3 and 4; Figure S8). Based on the study of Brenan (1994), solid-state diffusion of fluorine in the crystallites is not expected to be an efficient process in the range of alteration conditions investigated here, e.g. 3 weeks at 20 and 70°C, even though the defective nature of biologic apatite might facilitate chemical diffusion with respect to well-crystallised samples. Several observations also reveal significant changes pointing to the formation of a secondary phase. These changes include the observation of HPO_4^{2-} groups and modification of $^{18}O_{phosphate}$ value in the samples reacted with phosphate buffered solutions, as well as the formation of the (CO_3^{2-}, F^-) defect in some of the reacted samples. However, the lack of extensive narrowing of v_1 PO_4 bands and ^{19}F NMR signals in altered bone samples also suggests that dissolution and reprecipitation of a new phase is an incomplete process.

Based on these considerations, the v_1 PO_4 Ge ATR-FTIR bands were fitted using a two-component model. One of the component is a Gaussian function, whose position and width were kept fixed to that of the unaltered bone TH1. The second component is described by a Lorentzian function whose position was kept fixed to that of the reference carbonated fluorapatite sample in fluorinated samples and was let free in non-fluorinated samples (Figure 3). Assuming that extinction coefficients for the v_1 PO_4 band are similar in both phases, it is expected that the relative proportion of these two spectroscopic contributions match the fraction of PO_4 groups occurring in the primary and secondary apatite. Thus, it should reflect the relative molar proportions of both phases. In fluorinated samples, percentages of the secondary phase are about 60 % in samples altered at 70°C (D', E', F', G') and 30% in the sample altered at 20°C. In non-fluorinated samples, the second component is observed at 962.7-963.5 cm^{-1} and

accounts for 19 to 57 % of the total ν_1 PO$_4$ Ge ATR band. Consistently, the frequency of the ν_1 PO$_4$ band reported as a function of the fraction of secondary apatite broadly defines two distinct linear trends depending on the presence or absence of fluorine (Figure 8). For fluorinated samples, the linear trend points to the frequency of the reference carbonated fluorapatite whereas for the other samples it points to a frequency slightly above that of hydroxylapatite (962.9 cm^{-1}, from Balan et al., 2011 and Aufort et al., 2016). For fluorinated samples, the F concentration reported as a function of secondary apatite fraction also supports a mixing model involving the starting material and newly formed fluorapatite displaying an almost full-occupancy of the apatite channel sites by fluorine. Almost full channel occupancy in the secondary phase is also consistent with the corresponding very weak OH signal observed in the ^{1}H NMR spectra.

This set of observations supports the precipitation of a secondary phase induced by a partial dissolution of the original bioapatite in all reacted bone samples. It is noteworthy that the secondary apatite can consist in fluorapatite or hydroxylapatite, depending on the composition of the altering aqueous solution. Accordingly, fluorine does not appear to be a key element driving the transformation of bone apatite. However, fluorinated samples tend to display a larger proportion of secondary apatite, suggesting a higher rate of transformation. A higher precipitation rate of fluorapatite is expected due to its lower solubility and corresponding larger chemical affinity of the precipitation reaction compared to that of hydroxylapatite (Elliott 2002). In both instances, the driving force of the transformation is likely the solubility difference between the secondary phase and the more soluble bioapatite. While in the fluorinated samples the formation of carbonated fluorapatite is driven by its lower solubility compared to that of bioapatite (Kolodny, 1996; Trueman and Tuross, 2002), the replacement of bioapatite by a less carbonated and more hydroxylapatite-rich phase in the case of bones samples altered without fluorine, could be driven by the lower solubility of hydroxylapatite compared to that of carbonated bioapatite (Berna et al. 2004). Another feature emerging from the present series of experiments is an apparent maximum advancement of the transformation reaction, with a fraction of secondary apatite limited at ~60%. Note that an estimate of the fraction of secondary fluorapatite can also be inferred from the fluorine content measured in the fluorinated bone powders. Indeed, by considering that pure fluorapatite contains 3.77 wt.% F, the fluorinated samples with F contents ranging from 2.0 to 2.5 wt.% should consist of about 48 to 61 % of fluorapatite, which supports the findings from the ν_1 PO$_4$ band decomposition. The limited range of transformation, irrespective of the alteration conditions, suggests that the

secondary phase could have a protecting role against their further transformation. Thus, it is likely that the formation of secondary apatite occurs at the surface of initial grains. The degradation degree of the collagen matrix, inferred from amide bands in ATR-FTIR spectra and the signals ascribed to carboxylic functions and aliphatic carbons in ^{13}C NMR spectra, does not seem to affect the advancement of the apatite transformation.

4.2. Carbonate incorporation in secondary apatite

The oxygen and carbon isotopic compositions of structural carbonate groups from fossil apatites are important proxies for palaeo-environmental reconstructions. The behaviour of carbonate groups during aqueous alteration of teeth and bones thus deserves a special attention. In the present study, the overall decrease in the ν_2CO_3 band intensity of reacted samples, suggests that the secondary apatite phase is depleted in carbonate compared to the initial material. However, several observations also indicate that it is not carbonate-free.

In the fluorinated samples, the (CO_3^{2-}, F^-) defect is readily identified from its specific vibrational and NMR spectroscopic properties. Such atomic-scale modification of the environment of carbonate groups substituted for phosphate groups is a strong indication of their incorporation during the precipitation of the secondary apatite from the solution. In an ion-by-ion attachment model of crystal growth, incorporation at the B-site involves a competition between PO_4 and CO_3 groups. A high concentration of phosphate in solution is thus expected to inhibit carbonate incorporation at the B-site, precluding the formation of the clumped defect in phosphate buffered solutions.

In the absence of (CO_3^{2-}, F^-) defect, the ν_2CO_3 band reveals little modification of the carbonate environment or A-type to B-type ratio, which could suggest that only structural carbonate groups initially present in the bone apatite are preserved in these reacted samples. However, the oxygen and carbon isotopic compositions of structural carbonates contradict this interpretation. The lower $\delta^{13}C$ values of bones altered in a phosphate buffer (C, C', D, D') suggest incorporation of organic carbon, characterised by lower $^{13}C/^{12}C$ ratios (typically $\sim$ - 20 ‰, Lee-Thorp et al., 1989; Koch, 1998) than apatite structural carbonate, likely originating from the degradation of the collagen matrix. This is consistent with the significant loss of the signal corresponding to carboxylic functions observed in ^{13}C NMR for D and D' samples. The oxygen isotopic composition also reveals system opening. Samples tend to display a broad negative correlation as a function of secondary apatite fraction. Contrary to phosphate, oxygen exchange between carbonate in solution and water molecules occurs rapidly (Wang and

Cerling, 1994, Lécuyer et al., 1999; Geisler et al., 2012). Consequently, the variation of the $\delta^{18}O_{carbonate}$ values combined with almost constant $\delta^{13}C$ in samples altered in alkaline or organic buffer conditions, where the relative preservation of the organic matrix limits the incorporation of lighter organic carbon, could reflect a partial re-incorporation of carbonate during the transformation of apatite via dissolution and reprecipation from solution. It is noteworthy that the carbon and oxygen isotope compositions of structural carbonates in samples altered in alkaline conditions display similar variations irrespective of the presence or absence of fluorine, suggesting re-incorporation of carbonate groups in similar quantities.

4.3. Comparison of infrared and Raman spectroscopy in the determination of apatite structural order

Structural changes of fossil apatite are often characterized by crystallinity indices obtained from infrared spectroscopy, Raman spectroscopy or X-ray diffraction. Although usually displaying similar trends, these indices are often poorly correlated because they differ in physical nature (Rogers and Daniels, 2002; Pucéat et al., 2004; Trueman, 2008; Thompson et al., 2009). In the present study, a special attention was given to the use of ν_1 PO_4 Ge ATR-FTIR band to infer the degree of transformation of reacted samples. In previous studies (e.g. Pasteris and Ding, 2009; Pucéat et al., 2004), the ν_1 PO_4 bands observed in Raman spectroscopy were also used to infer the structural state of experimentally or naturally altered biogenic apatite samples. It is thus relevant to compare the information obtained from IR and Raman spectroscopy using closely related vibrational modes. We note, however, that in crystalline apatite the intense ν_1 PO_4 signal observed in the Raman spectrum is related to a A irreducible representation. It differs from the vibrational mode belonging to a E irreducible representation and corresponding to the weak ν_1 PO_4 signal of the IR spectrum (Leroy et al., 2000; Ulian and Valdrè, 2018). Both types of vibrational modes however display very close frequencies. In the present study, the position of the ν_1 PO_4 Ge ATR-FTIR band correlates well with that of the Raman ν_1 PO_4 (Figure 9a), both spectroscopies showing the same extent of frequency shift from non-fluorinated to fluorinated bone samples. However, Raman and Ge ATR-FTIR FWHM do not correlate well (Figure 9b). Indeed, the ν_1 PO_4 Raman peaks are narrower and more symmetric than their Ge ATR-FTIR counterparts, the Raman asymmetry parameters being about half that of ATR-FTIR peaks (Figure 9c). This difference could be related to the observation that the Raman intensity is more strongly affected by structural distortions than the infrared one (Ulian and Valdrè, 2018). As a consequence, the smaller carbonate content of secondary apatite might lead to an increase in its Raman scattering efficiency, leading to an

overexpression of its contribution in the Raman spectra. Correspondingly, the ν_1 PO$_4$ Raman peaks appear as narrower and more symmetric than their infrared counterparts do. These observations illustrate how the physical processes involved in related but different probing techniques can affect the determination of sample structural order.

4.4. Implications for fossilisation processes

This work has implications regarding bone diagenetic processes and stable isotopes analysis of fossil bioapatite. Our results are consistent with the observations that the relative importance of dissolution/recrystallisation processes during diagenesis, not only depends on the bone microstructure but also on the physical–chemical conditions prevailing in the fossilisation environments (Berna et al., 2004; Pfretzschner, 2004; Trueman et al., 2004, Zazzo et al., 2004b). As far as palaeoenvironmental reconstructions based on stable isotope analysis of bioapatites are concerned, the nature of ionic species in percolating fluids in contact with fossils could be key parameters driving the preservation or alteration of isotopic compositions. Importantly, dissolution-recrystallisation of bone can occur in a fluorine-free environment to form secondary carbonated hydroxylapatite. This suggests that other factors drive the transformation of bone, such as the reactivity of a disordered surface layer on bone crystallites (e.g. Wang et al., 2013) and a high carbonate content (Hankermeyer et al., 2002). The fact that alteration of the original bioapatite is possible without a significant variation of the A-type to B-type carbonate ratio points to a limit of single-analytical approaches in assessing bone diagenesis. In addition, it does not exclude possible reincrodorporation of carbonate into the structure, which makes the assessment of isotopic compositions preservation more complex. This could explain why several studies reported that indicators of diagenesis indicated little about isotope alteration (e.g. Trueman et al., 2008).

The dissolution-recrystallization process of bone is incomplete with a maximum fraction of secondary apatite limited to ~60 %. It is thus suggested that partial transformation of bone occurs even at a nanometric scale with partial dissolution-recrystallisation of individual crystallites (Figure 10). However, it is noteworthy that the chemical changes observed between the primary and secondary phases are not compatible with the premise of Ostwald ripening process even though this mechanism has been proposed to account for dissolution of smaller crystallites and formation of larger crystals (Ayliffe et al., 1994). The formation of a secondary phase and the lack of increase in MCD size in altered bones observed in this study points primarily to a chemically driven transformation rather than a surface driven ripening process.

Compared to modern unaltered bone, artificially fluorinated bone samples in organic buffers or in alkaline conditions show similar transformations as fossils: degradation of organic content, increase in crystallinity (e.g. increase in IRSF values), formation of carbonated fluorapatite (i.e. clumped defect at B-site). In fossil enamel from late Tertiary continental environments, such a transformation of bioapatite to carbonated fluorapatite has been shown to occur via a dissolution-recrystallisation process, with extensive alteration of the carbonate environment (Yi et al., 2014). The relative preservation of the chemical and structural environment of the carbonate groups in altered bone powders is consistent with a subtler transformation mechanism, compatible with a partial dissolution-recrystallisation process operating at nanometer-size scale.

Compared to actual fossilisation environments, the alteration experiments conducted here on modern bone samples have been performed in a closed system and can be expected to become chemically self-buffered fairly quickly. In comparison, actual fossilisation environments rather lead to an open-system behaviour where the bone material is slowly altered by the repeated passage of new aqueous fluids over geological times. However, atomic scale transformation of fossil bones from late Miocene deposits of Kenya and Plio-Pleistocene deposits of South Africa also points to a partial dissolution-recrystallization process (Aufort et al., 2019). This could indicate that, also in nature, a closing of the system could occur after a certain amount of time. Accordingly, fossil bones could record the physical-chemical conditions prevailing in their early fossilisation environments. This points to a key role of the secondary phase formation as a limiting factor of the transformation process and begs the question of its potential protective role against total dissolution of the primary bioapatite.

Finally, this work illustrates that bone diagenesis cannot be summed up using only one crystallinity parameter and underlines the need to use multiple analytical approaches to depict a more complete picture of the extent of diagenetic alteration in bone. Furthermore, this shows that the combination of site-specific isotopic compositions measurements with atomic scale-probing spectroscopies is an effective way of deciphering dissolution-recrystallisation pathways in bone.

5. Conclusions

This study provides a quantitative assessment of the mineralogical transformations at the atomic scale and stable isotopic changes during *in vitro* alteration experiments of bone bioapatite. Partial dissolution of the biogenic apatite and recrystallization of a carbonate-bearing secondary

apatite was observed in all bone samples altered in aqueous solutions at 20 and 70°C. This transformation occurs irrespective of the presence or absence of fluorine in solution and leads to the formation of carbonate-bearing fluorapatite or carbonate-bearing hydroxylapatite respectively. An ATR-FTIR based estimate of this transformation revealed that the fraction of newly formed secondary apatite was limited to about 60%. This result could point to a protective role of the secondary apatite against total dissolution of the primary bioapatite. On a more general note, this work also contributes to the debate surrounding the passivation capacity of secondary phases (e.g. Velbel, 1993; Daval et al., 2011; Daval et al. 2013; Sissmann et al., 2013; Harrison et al. 2015), relevant to a variety of geochemical contexts involving mineral replacement reactions through dissolution-recrystallization processes at the solid/solution interface.

References

Amiot, R., Lécuyer, C., Buffetaut, E., Fluteau, F., Legendre, S., Martineau, F. 2004. Latitudinal temperature gradient during the Cretaceous Upper Campanian – Middle Maastrichtian: $\delta^{18}O$ record of continental vertebrates. Earth and Planetary Science Letters 226, 255–272.

Apfelbaum, F., Diab, H., Mayer, I., Featherstone, J.D.B. 1992. A FTIR study of carbonate in synthetic apatites. Journal of inorganic biochemistry 45, 277-282.

Arends, J. and Davidson, C.L. 1974. HPO_4^{2-} content in enamel and artificial carious lesions. Calcified Tissue Research 18 65-79.

Aufort, J., Lebon, M., Gallet, X., Ségalen, L., Gervais, C., Brouder, C., Balan, E. 2018. Macroscopic electrostatic effects in ATR-FTIR spectra of modern and archaeological bones. American Mineralogist 103, 326-329

Aufort, J., Ségalen, L., Gervais, C., Brouder, C., Balan, E. 2016. Modeling the attenuated total reflectance infrared (ATR-FTIR) spectrum of apatite. Physics and Chemistry of Minerals 43, 615-626.

Aufort, J., Gommery, D., Gervais, C., Ségalen, L., Labourdette, N., Coelho-Diogo, C., Balan, E., 2019. Assessing bone transformation in late Miocene and Plio-Pleistocene deposits of Kenya and South Africa. Archaeometry, DOI: 10.1111/arcm.12471.

Ayliffe, L.K., Chivas, A.R., Leakey, M.G., 1994. The retention of primary oxygen isotope compositions of fossil elephant skeletal phosphate. Geochimica et Cosmochimica Acta 58, 5291–5298.

Balan, E., Delattre, S., Roche, D., Segalen, L., Morin, G., Guillaumet, M., Blanchard, M., Lazzeri, M., Brouder, C., Salje, E.K.H., 2011. Line-broadening effects in the powder infrared spectrum of apatite, Physics and Chemistry of Minerals 38, 111-122.

Balan, E., Aufort, J., Saldi, G.D., Brouder C., Lazzeri, M., 2019. Line-broadening and anharmonic effects in the attenuated total reflectance infrared spectra of calcite. European Journal of Mineralogy, 31, 73-81.

Berna, F., Matthews, A., Weiner, S., 2004. Solubilities of bone mineral from archaeological sites: The recrystallization window. Journal of Archaeological Science 31, 867-882.

Brenan, J., 1994. Kinetics of fluorine, chlorine and hydroxyl exchange in fluorapatite (1994) Chemical Geology 110, 195-210.

Cerling, T.E., Harris, J.M., 1999. Carbon isotope fractionation between diet and bioapatite in ungulate mammals and implications for ecological and paleoecological studies. Oecologia 120, 347–363.

Cerling, T.E., Harris, J.M., Leakey, M.G., 1999. Browsing and grazing in elephants: the isotope record of modern and fossil proboscideans. Oecologia 120, 364–374.

Crowson, R.A., Showers, W.J., Wright, E.K., Hoering, T.C., 1991. Preparation of phosphate samples for oxygen isotope analysis. Anal Chem 63, 2397–2400

Chadefaux, C., Le Hô, A.-S., Bellot-Gurlet, L., Reiche, I., 2009. Curve-fitting micro-ATR-FTIR studies of the amide I and II bands of type I collagen in archaeological bone materials. E-Preservation Science 6, 129–137.

Chevrinais, M., Balan, E., Cloutier, R., 2015. New insights in the ontogeny and taphonomy of the Devonian acanthodian Triazeugacanthus affinis from the Miguasha fossil-Lagerstätte, Eastern Canada. Minerals 2016, 6, 1-17

Cho, G., Wu, Y., Ackerman, J.L., 2003. Detection of hydroxyl ions in bone mineral by solid-state NMR spectroscopy. Science 300, 1123-1127

Daval, D., Sissmann, O., Menguy, N., Saldi, G.D., Guyot, F., Martinez, I., Corvisier, J., Garcia, B., Machouk, I., Knauss, K.G., Hellman, R., 2011. Influence of amorphous silica layer formation on the dissolution rate of olivine at 90°C and elevated pCO_2. Chemical Geology 284, 193-209.

Daval, D., Hellman, R., Saldi, G.R., Wirth, R., Knauss, K.G., 2013. Linking nm-scale measurements of the anisotropy of silicate surface reactivity to macroscopic dissolution rate laws: New insights based on diopside. Geochemica and Cosmochimica Acta 107, 121-134.

DeNiro, M.J., Epstein, S., 1978. Influence of diet on the distribution of carbon isotopes in animals. Geochimica et Cosmochimica Acta 42, 495–506.

Elliott, J.C., 2002. Calcium phosphate biominerals. In: Kohn MJ, Rakovan J, Hughes JM (eds) Phosphates: Geochemical, Geobiological, and Material Importance. Reviews in Mineralogy & Geochemistry 48, pp 427-454

Fricke, H.C., Clyde, W.C., O'Neil, J.R. 1998. Intra-tooth variations in $\delta^{18}O$ (PO4) of mammalian tooth enamel as a record of seasonal variations in continental climate variables. Geochimica et Cosmochimica Acta 62, 1839-1850.

Geisler, T., Perdikouri, C., Kasioptas, A., Dietzel, M. 2012. Real-time monitoring of the overall exchange of oxygen isotopes between aqueous CO_3^{2-} and H_2O by Raman spectroscopy. Geochimica et Cosmochimica Acta 90, 1-11.

Glimcher MJ (2006) Bone: Nature of the calcium phosphate crystals and cellular, structural, and physical chemical mechanisms in their formation. In: Sahai N, Schoonen MAA (eds) Medical Mineralogy and Geochemistry. Reviews in Mineralogy & Geochemistry 64, pp 223-282

Harrison, A.L., Dipple, G.M., Power, A.M., Mayer, U., 2015. Influence of surface passivation and water content on mineral reactions in unsaturated porous media: Implications for brucite carbonation and CO2 squestration. Geochimica et Cosmochimica Acta 148, 477-495.

Hankermeyer, C.R., Ohashi, K.L., Delaney, D.C., Ross, J., Constantz, B.R. 2002. Dissolution rates of carbonated hydroxyapatite in hydrochloric acid. Biomaterials 23, 743-750.

Hedges, R.E.M., 2002. Bone diagenesis: an overview of processes. Archaeometry 44, 319–328.

Hut, G. 1987. Consultants' group meeting on stable isotope reference samples for geochemical and hydrological investigations. Accessible at : http://www.iaea.org/inis/collection/NCLCollectionStore/_Public/18/075/18075746.pdf.

Keenan, S.W., Engel, A.S., Roy, A., Bovenkamp-Langlois, G.L., 2015. evaluating the consequences of diagenesis and fossilization on bioapatite lattice structure and composition. Chemical geology 413, 18-27

Keenan, S.W., Engel, A.S., 2017. Early diagenesis and recrystallization of bone. Geochimica et Cosmochimica Acta 196, 209-223

Kim, S.-T., Mucci, A., Taylor, B.E., 2007. Phosphoric acid fractionation factors for calcite and aragonite between 25 and 75°C: Revisited. Chemical Geology 246, 135-146

Kingston, J.D., Harrison, T., 2007. Isotopic dietary reconstructions of Pliocene herbivores at Laetoli: implications for early hominin Paleoecology. Palaeogeography, Palaeoclimatology, Palaeoecology 243, 272–306.

Koch, P.L., 1998. Isotopic reconstruction of past continental environments. Annual Review of Earth and Planetary Sciences 26, 573-613

Kohn M.J. and Cerling T.E. (2002) Stable isotope compositions of biological apatite. In Kohn MJ, Rakovan J, and Hughes JM, Eds., Phosphates - Geochemical, geobiological and materials importance, vol 48, p. 455-488. Reviews in Mineralogy and Geochemistry, Mineralogical Society of America and Geochemical Society, Chantilly, Virginia

Kolodny, Y., Luz, B., Sander, M., Clemens, W.A., 1996. Dinosaur bones: fossils or pseudomorphs? The pitfalls of physiology reconstruction from apatitic fossils. Palaeogeography, Palaeoclimatology, Palaeoecology 126, 161-171

Kourkoumelis, N., Balatsoukas, I., Tzaphlidou, M., 2012. Ca/P concentration ratio at different sites of normal and osteoporotic rabbit bones evaluated by auger and energy dispersive X-ray spectroscopy. J. Biol. Phys. 38, 279-291

Lebon, M., Reiche, I., Gallet, X., Bellot-Gurlet, L., Zazzo, A., 2016. Rapid quantification of bone collagen content by ATR-FTIR spectroscopy. Radiocarbon 58, 131-145

Lécuyer, C., Grandjean, P., O'Neil, J.R., Cappetta, H., Martineau, F., 1993. Thermal excursions in the ocean at the Cretaceous—Tertiary boundary (northern Morocco): $\delta18O$ record of phosphatic fish debris Palaeogeography, Palaeoclimatology, Palaeoecology 105, 235-243

Lécuyer, C., Grandjean, P., Sheppard, S.M.F., 1999. Oxygen isotope exchange between dissolved phosphate and water at temperatures ≤135°C: Inorganic versus biological fractionations. Geochimica et Cosmochimica Acta 63, 855-862

Lécuyer C., Balter V., Martineau F., Fourel F., Bernard A., Amiot R., Gardien V., Otero O., Legendre S., Panczer G., Simon L., Martini R., 2010. Oxygen isotope fractionation between apatite-bound carbonate and water determined from controlled experiments with synthetic apatites precipitated at 10-37°C. Geochimica et Cosmochimica Acta 74, 2072-2081

Lee-Thorp, J.A., Sealy, J.C., van der Merwe, N.J., 1989. Stable carbon isotope ratio differences between bone collagen and bone apatite, and their relationship to diet. Journal of Archaeological Science 16, 585–599.

Lee-Thorp, J.A., Sponheimer, M., 2003. Three case studies used to reassess the reliability of fossil bone and enamel isotope signals for paleodietary studies. J. Anthropol. Archaeol. 22, 208–216.

Lee-Thorp, J.A., 2008. On isotopes and old bones. Archaeometry 50, 925-950

LeGeros, R.Z., LeGeros, J.P., 1984. Phosphate minerals in human tissue. In: Nriagu JO, Moore PB (eds) Phosphate Minerals. Springer-Verlag, New York, pp 351-395

LeGeros, R.Z., 1991. Calcium phosphates in oral biology and medicine, Karger, Paris

Leroy, G., Leroy, N., Penel, G., Rey, C., Lafforgue, P., Bres, E. 2000. Polarized micro-Raman study of fluorapatite single crystals. Applied Spectroscopy 54, 1521-1527

Levin, N.E., Cerling, T.E., Passey, B.H., Harris, J.M., Ehleringer, J.R., 2006. A stable isotope aridity index for terrestrial environments. Proceedings of the National Academy of Science 103, 11201–11205.

Longinelli, A., 1984. Oxygen isotopes in mammal bone phosphate: a new tool for paleohydrological and paleoclimatological research? Geochimica et Cosmochimica Acta 48, 385–390.

Loong, C.-K., Rey, C., Kuhn, T., Combes, C., Wu, Y., Chen, S.-H., Glimcher, M.J. 2000. Evidence of hydroxyl ion deficiency in bone apatites: an inelastic neutron scattering study. Bone 26, 599-602

Maurer, A.F., Gerard, M., Person, A., Barrientos, I., del Carmen Ruiz, P., Darras, V., Durlet, C., Zeitoun, V., Renard, M., Faugère, B., 2011. Intra-skeletal variability in trace elemental content of Precolumbian Chupicuaro human bones: the record of post-mortem alteration and a tool for palaeodietary reconstruction. Journal of Archaeological Science 38, 1784-1797

Michel V., Ildefonse P., Morin G. 1995. Chemical and structural changes in Cervus elaphus tooth enamels during fossilization (Lazaret cave): a combined IR and XRD Rietveld analysis. Applied Geochemistry 10, 145-159

Millard, A.R., Hedges, R.E.M., 1996. A diffusion-adsorption model of uranium uptake by archaeological bone. Geochim Cosmochim Acta 60, 2139–2152.

Morin, G., Allard, T., Balan, E., Ildefonse, P., Calas, G., 2002. Native Cd^+ in sedimentary fluorapatite. European Journal of Mineralogy 14, 1087–1094

Nakano, T., Tokumura, A., Umahoshi, Y., 2002. Variation in crystallinity of hydroxyapatite and the related calcium phosphates by mechanical grinding and subsequent heat treatment. Metallurgical and Materials transactions A 33, 521-528.

Passey, B.H., Robinson, T.F., Ayliffe, L.K., Cerling, T.E., Sponheimer, M., Dearing, M.D., Roeder, B.L., Ehleringer, J.M. 2005. Carbon isotope fractionation between diet, breath CO2, and bioapatite in different mammals. Journal of Archaeological Science 32, 1459–1470.

Pasteris, J.D., Wopenka, B., Freeman, J.J., Rogers, K., Valsami-Jones, E., van der Houwen, J.A.M., Silva, M.J., 2004. Lack of OH in nanocrystalline apatite as a function of degree of atomic order: implications for bone and biomaterials. Biomaterials 25, 229-238.

Pasteris, J.D., Wopenka, B., Valsami-Jones, E., 2008. Bone and tooth mineralization: why apatite? Elements 4, 97–104.

Pasteris, J.D., Ding, D.Y., 2009. Experimental fluoridation of nanocrystalline apatite. American Mineralogist 94, 53-63.

Person, A., Bocherens, H., Saliège, J.-F., Paris, F., Zeitoun, V. and Gérard, M., 1995. Early diagenetic evolution of bone phosphates: a X-ray diffractometry analysis. Journal of Archaeological Science 22, 211-221.

Pfretzschner, H-U., 2004. Fossilization of Haversian bone in aquatic environments. C.R. Palevol 3, 605-616.

Pucéat, E., Reynard, B., Lécuyer, C., 2004. Can crystallinity be used to determine the degree of chemical alteration of biogenic apatites? Chemical Geology 205, 83–97.

Putnis, A., 2002. Mineral replacement reactions: from macroscopic observations to microscopic mechanisms. Mineralogical Magazine 66, 689-708.

Putnis, A., Putnis, C.V. (2007) The mechanism of reequilibration of solids in the presence of a fluid phase. Journal of Solid State Chemistry 180, 1783-1786.

Reiche, I., Favre-Quattropani, L., Vignaud, C., Bocherens, H., Charlet, L., Menu, M., 2003. A multi-analytical study of bone diagenesis: the Neolithic site of Bercy (Paris, France). Meas. Sci. Technol., 14, 1608-1619.

Rey C., Lian J., Grynpas M., Shapiro F., Zylberberg L., Glimcher M.J. (1989) Non-apatitic environments in bone mineral: FT-IR detection, biological properties and changes in several disease states. Conn Tissue Research 21, 267-273

Reynard, B., Balter, V., 2014. Trace elements and their isotopes in bones and teeth: Diet, environments, diagenesis, and dating of archeological and paleontological samples. Palaeogeography, Palaeoclimatology, Palaeoecology 416, 4-16.

Roche, D., Ségalen, L., Balan, E., Delattre, S., 2010. Preservation assessment of Miocene-Pliocene tooth enamel from Tugen Hills (Kenyan Rift Valley) through FTIR, chemical and stable-isotope analyses. Journal of Archaeological Science 37 1690-1699.

Roche, D., Ségalen, L., Senut, B., Pickford, M., 2013. Stable isotope analysis of tooth enamel carbonate of large herbivores from the Tugen Hills deposits: palaeoenvironmental context of the earliest Kenyan hominids. Earth and Planetary Science Letters 381, 39-51.

Rodriguez-Carvajal, J., 1993. Recent advances in magnetic structure determination by neutron powder diffraction. Physica B: Condensed Matter 192, 55-69.

Rogers, K.D., and Daniels, P., 2002. X-ray diffraction of the effects of heat treatment on bone mineral microstructure. Biomaterials 23, 2577-2585.

Sharp, Z.D., Atudorei, V., Furrer, H., 2000. The effect of diagenesis on oxygen isotope ratios of biogenic phosphates. Am J Sci 300, 222-

Shemesh, A., 1990. Crystallinity and diagenesis of sedimentary apatites. Geochimica et Cosmochimica Acta, 54, 2433-2438.

Sillen, A., and LeGeros, R., 1991. Solubility profiles of synthetic apatites and of modern and fossil bones. Journal of Archaeological Science, 18, 385-397.

Sillen, A., and Morris A., 1996. Diagenesis of bone from Border Cave: implications for the age of the Border Cave hominids. Journal of Human evolution, 31, 499-506.

Sissmann, O., Daval, D., Brunet, F., Guyot, F., Verlaguet, A., Pinquier, Y., Findling, N., Martinez, I., 2013. The deleterious effect of secondary phases on olivine carbonation yield: Insight from time-resolved aqueous-fluid sampling and FIB-TEM characterization. Chemical Geology 357, 186-202.

Sponheimer, M., and Lee-Thorp, J., 1999. Alteration of enamel carbonate environments during fossilization. Journal of Archaeological Science, 26, 143-150.

Surovell, T.A., Stiner, M.C., 2001. Standardizing infrared measures of bone mineral crystallinity: an experimental approach. Journal of Archaeological Science 28, 633-642.

Thompson, T.J.U., Gauthier, M., Islam, M., 2009. The application of a new method of Fourier Transform Infrared spectroscopy to the analysis of burned bone. Journal of Archaeological Science 36, 910-914.

Trueman C.N. and Tuross N. 2002. Trace elements in recent and fossil bone apatite. In MJ Kohn, J Rakovan, and JM Hughes, Eds., Phosphates - Geochemical, geobiological and materials importance, vol 48, p. 489-521. Reviews in Mineralogy and Geochemistry, Mineralogical Society of America and Geochemical Society, Chantilly, Virginia

Trueman, C.N.G., Behrensmeyer, A.K., Tuross, N., Weiner, S., 2004. Mineralogical and compositional changes in bones exposed on soil surfaces in Amboseli National Park, Kenya: diagenetic mechanisms and the role of sediment pore fluids. J Archaeol Sci 31, 721–39.

Trueman, C.N., Privat, K., Field, J. 2008. Why do crystallinity values fail to predict the extent of diagenetic alteration of bone mineral? Palaeogeography, Palaeoclimatology, Palaeoecology, 266, 160-167.

Tütken T., Vennemann T.W., Pfretzschner H.-U. 2008. Early diagenesis of bone and tooth apatite in fluvial and marine settings: Constraints from combined oxygen isotope, nitrogen and REE analysis. Palaeogeography, palaeoclimatology, palaeoecology 266, 254-268

Ulian, G., Valdrè, G., 2018. Effect of mechanical stress on the Raman and infrared bands of hydroxylapatite: A quantum mechanical first principle study. Journal of the Mechanical Behaviour of Biomedical Materials 77, 683-692.

Velbel, M.A., 1993. Formation of protective surface layers during silicate-mineral weathering under well-leached, oxidizing conditions. American Mineralogist 78, 405-414.

Wang, Y., Cerling, T.E., 1994. A model for fossil tooth and bone diagenesis: implications for paleodiet reconstruction from stable isotopes. Palaeogeography, Palaeoclimatology, Palaeoecology 107, 596–606.

Wang, L., Putnis, C.V., Ruiz-Agudo, E., King, H.E., Putnis, A., 2013. Coupled dissolution and precipitation at the cerussite-phosphate solution interface: implications for immobilization of lead in soils. Environmental Science and Technology 47, 13502-13510.

Wang, Y., Von Euw, S., Fernandes, F.M., Cassaignon, S., Selmane, M., Laurent, G., Pehau-Arnaudet, G., Coelho, C., Bonhomme-Coury, L., Giraud-Guille, M.-M., Babonneau, F., Azaïs, T., Nassif, N., 2013. Water-mediated structuring of bone apatite. Nature materials 12, 1144-1153.

Weiner, S. and Bar-Yosef, O., 1990. States of preservation of bones from prehistoric sites in the Near East: a survey. Journal of Archaeological Science 17, 187-196.

Wopenka, B., and Pasteris, J.D., 2005. A mineralogical perspective on the apatite in bone Materials Science and Engineering C 25, 131-143.

Yi, H., Balan, E., Gervais, C., Segalen, L., Fayon, F., Roche, D., Person, A., Morin, G., Guillaumet, M., Blanchard, M., Lazzeri, M., Babonneau, F., 2013. A carbonate-fluoride defect model for carbonate-rich fluorapatite. Am Mineral 98**,** 1066-1069.

Yi, H., Balan, E., Gervais, C., Segalen, L., Roche, D., Fayon, F., Person, A., Morin, G., Babonneau, F., 2014. Probing atomic scale transformation of fossil enamel using FTIR and NMR spectroscopy: A case study from the Tugen Hills (Rift Gregory, Kenya). Acta Biomaterialia, 10, 3952-3958.

Zazzo, A., Lécuyer, C., Sheppard, S.M.F., Grandjean, P., Mariotti, A., 2004a. Diagenesis and the reconstruction of paleoenvironments A method to restore original $\delta^{18}O$ values of carbonate and phosphate from fossil tooth enamel Geochimica et Ccosmochimica Acta 68, 2245-2258.

Zazzo, A, Lécuyer, C, Mariotti, A., 2004b. Experimentally-controlled carbon and oxygen isotope exchange between bioapatites and water under inorganic and microbially-mediated conditions. Geochim Cosmochim Acta 68, 1–12.

Table 1 Alteration conditions of bone wafers and powders. For each experiment, the prime symbol refers to the fluorinated bone sample.

Exp.	Sample type	Duration	Temperature (°C)	pH	Solution	[NaF]
A	Wafer	1 week	20	7	Phosphate	-
A'	"	"	"	"	"	10^{-2}M
C	Powder	3 weeks	20	7	Phosphate	-
C'	"	"	"	"	"	10^{-2}M
D	Powder	3 weeks	70	7	Phosphate	-
D'	"	"	"	"	"	10^{-2}M
E	Powder	3 weeks	70	7	PIPES	-
E'	"	"	"	"	"	10^{-2}M
F	Powder	3 weeks	70	9	KOH	-
F'	"	"	"	"	"	10^{-2}M
G	Powder	3 weeks	70	10	KOH	-
G'	"	"	"	"	"	10^{-2}M
H	Wafer	3 weeks	70	7	PIPES	-
H'	"	"	"	"	"	10^{-2}M

Table 2 Fluorine content, Ca/P molar ratio and isotopic composition of unaltered, control and fluorinated bones.

Sample	F (%)	Ca/P	$\delta^{13}C$ (‰PDB)	$\delta^{18}O_{carbonate}$ (‰VSMOW)	$\delta^{18}O_{phosphate}$ (‰VSMOW)
TH1	0.20	1.57	-6.41 ± 0.20	36.31 ± 0.14	25.80 ± 0.39
C	0.23	1.66	-7.06 ± 0.02	36.19 ± 0.68	21.61 ± 0.81
C'	1.6	1.64	-7.22 ± 0.09	37.42 ± 0.02	22.65 ± 0.25
D	0.23	1.70	-7.27 ± 0.04	35.17 ± 0.19	21.18 ± 0.14
D'	2.0	1.72	-6.97 ± 0.02	36.88 ± 0.15	20.45 ± 0.13
E	0.24	1.79	-6.38 ± 0.01	33.95 ± 0.30	26.49 ± 0.17
E'	2.5	1.81	-6.50 ± 0.01	35.29 ± 0.27	26.38 ± 0.56
F	0.26	1.84	-6.50 ± 0.07	34.05 ± 0.19	26.94 ± 0.61
F'	2.2	1.82	-6.42 ± 0.01	33.15 ± 0.12	26.81 ± 0.42
G	0.24	1.86	-6.43 ± 0.01	33.55 ± 0.36	26.28 ± 0.38
G'	2.1	1.84	-6.52 ± 0.12	32.83 ± 0.23	27.03 ± 0.40

Table 3 Lattice parameters (P6₃/m), average apparent size and strain from Le Bail fits of XRD data

Sample	a (Å)	c (Å)	Volume (Å)	Crystallite size (Å) [002]	[030]	Average microstrain (anisotropy)
TH1	9.4173 (6)	6.8756 (5)	528.07 (6)	776.53	126.90	85.91 (0.094)
C'	9.4035 (3)	6.8870 (3)	527.40 (3)	308.31	114.45	31.62 (0.079)
D	9.4219 (2)	6.8867 (3)	529.44 (3)	397.58	115.30	33.74 (0.055)
D'	9.3916 (2)	6.8848 (2)	525.90 (2)	427.53	140.90	25.28 (0.062)
E	9.4155 (2)	6.8892 (3)	528.91 (3)	319.27	117.25	24.11 (0.073)
E'	9.3826 (2)	6.8879 (2)	525.13 (2)	548.21	146.92	25.41 (0.040)
F	9.4133 (3)	6.8913 (3)	528.84 (4)	441.28	120.53	39.39 (0.043)

F'	9.3777 (2)	6.8908 (2)	524.80 (2)	442.84	137.16	24.14 (0.078)
G	9.4120 (3)	6.8896 (3)	528.55 (3)	491.76	106.48	33.79 (0.047)
G'	9.3809 (2)	6.8924 (2)	525.28 (2)	520.14	141.08	27.66 (0.037)

Table 4 Parameters obtained from the ν_1 PO_4 band in Ge ATR-FTIR spectra. In addition to the Full Width at Half Maximum (FWHM), we calculated the Half Width at Half Maximum (HWHM) on the high frequency side, the low frequency side exhibiting a pronounced asymmetry. The asymmetry parameter is then defined as $1 - 2(HWHM/FWHM)$. An asymmetry parameter equal to zero corresponds to a perfectly symmetrical band, an increase in the parameter corresponds to an increase in asymmetry. The IR Splitting Factor (IRSF) was calculated from the ν_4 PO_4 Ge ATR-FTIR band, according to Weiner and Bar-Yosef (1990). Parameters related to the Raman ν_1 PO_4 peak, i.e. position, FWHM and asymmetry, are also reported.

Sample	Ge ATR-FTIR					Raman		
	ν_1 PO_4				ν_4 PO_4	ν_1 PO_4		
	ω (cm^{-1})	FWHM (cm^{-1})	HWHM (cm^{-1})	Asymmetry	IRSF	ω (cm^{-1})	FWHM (cm^{-1})	Asymmetry
TH1	960.6	15.1	6.86	0.091	3.64	960.5	15.6	0.051
C	961.3	15.5	6.83	0.119	3.89	960.7	13.6	0.060
C'	962.1	15.3	6.10	0.203	4.00	963.2	11.9	0.116
D	961.2	15.5	6.40	0.174	4.56	961.4	11.6	0.088
D'	963.7	15.1	5.68	0.248	5.03	963.9	10.1	0.129
E	961.7	13.3	5.57	0.162	4.28	961.6	11.6	0.088
E'	964.1	12.8	4.50	0.297	5.11	964.3	9.2	0.150
F	962.0	13.5	5.91	0.124	4.53	961.6	12.8	0.064
F'	964.0	12.7	4.56	0.282	5.88	963.9	10.0	0.140
G	962.0	15.3	6.35	0.170	4.55	961.7	13.4	0.063
G'	964.3	12.0	4.80	0.200	5.19	964.2	10.3	0.136
C-Fap	966.1	5.2	-	-	6.18	-	-	-

Table 5 Parameters of the fit of the OH signal in ^{1}H NMR spectra of control and fluorinated bones.

Sample	Amplitude (a.u.)	Position (ppm)	Width (ppm)	%$_{remaining OH signal}$
C	2.07	-0.034	0.53	
C'	0.23	-0.034	0.53	12
D	4.43	-0.063	0.45	
D'	0.37	-0.063	0.45	8
E	3.49	-0.028	0.32	
E'	0.14	-0.028	0.32	4
F	1.01	-0.018	0.36	
F'	0.09	-0.018	0.36	9

Table 6 Parameters of multi-component fits of $\nu_1 PO_4$ Ge ATR-FTIR bands. It is expected that the relative proportion of the Lorentzian component reflects that of the structural phosphate groups belonging to the recrystallised secondary apatite and that the fraction corresponding to the Gaussian component reflects that of the structural phosphate groups belonging to the primary bioapatite.

Sample	"TH1-like" Gaussian signal			Secondary Lorentzian contribution		
	ω (cm^{-1})	Width	Area (%)	ω (cm^{-1})	FWHM	Area (%)
TH1	960.6	8.755	100	-	-	-
C	960.6	8.755	80.9 ± 3.9	962.7	7.901	19.1 ± 2.4
C'	960.6	8.755	70.6 ± 3.1	966.1	8.000	29.4 ± 2.5
D	960.6	8.755	70.5 ± 8.5	963.5	10.553	29.5 ± 7.2
D'	960.6	8.755	43.2 ± 1.2	966.1	9.530	56.8 ± 2.0
E	960.6	8.755	60.9 ± 6.3	962.9	7.025	39.1 ± 5.6
E'	960.6	8.755	41.4 ± 1.9	966.1	7.971	58.6 ± 2.9
F	960.6	8.755	47.3 ± 7.5	963.4	8.566	52.7 ± 9.0
F'	960.6	8.755	43.1 ± 2.7	966.1	7.585	56.9 ± 4.1
G	960.6	8.755	43.3 ± 4.4	963.4	11.748	56.7 ± 6.1
G'	960.6	8.755	38.5 ± 3.0	966.1	7.603	61.5 ± 4.4
C-FAp	-	-	-	966.1	5.357	100

Figure 1 a. $\delta^{18}O_{carbonate}$ of the unaltered and artificially altered bone samples reported against their $\delta^{18}O_{phosphate}$ values and compared with the linear correlation derived by Lécuyer et al. (2010) from compiled data of $\delta^{18}O$ values of both carbonate and phosphate from modern mammals (solid line) and with the linear correlation derived by Zazzo et al. (2004b) from modern hippopotamuses. **b.** $\delta^{13}C$ values of the unaltered and artificially altered bones. Red and blue circles correspond to non-fluorinated and fluorinated bone samples respectively.
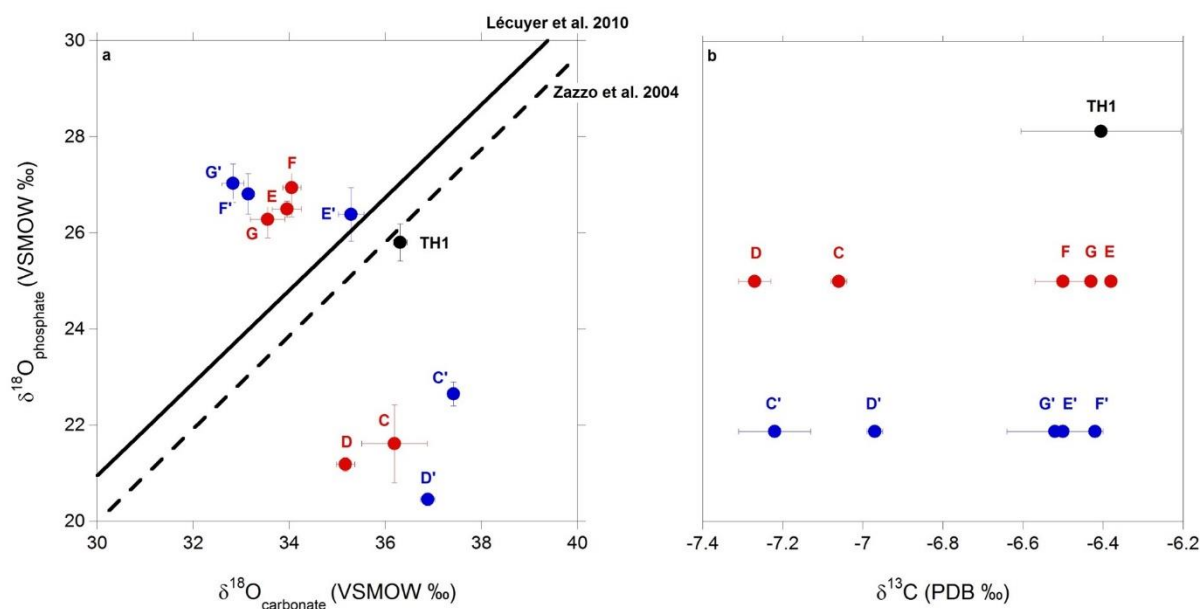
Figure 2 Diamond and Ge ATR FTIR spectra of the modern ox bone used in all alteration experiments, TH1. For better comparison, spectra are shifted vertically and the intensity of the Ge ATR spectrum was multiplied by the factor three.
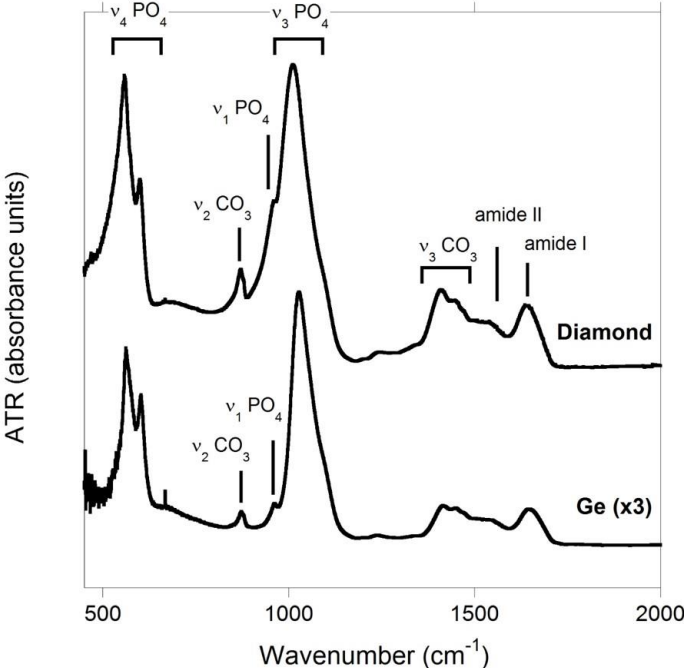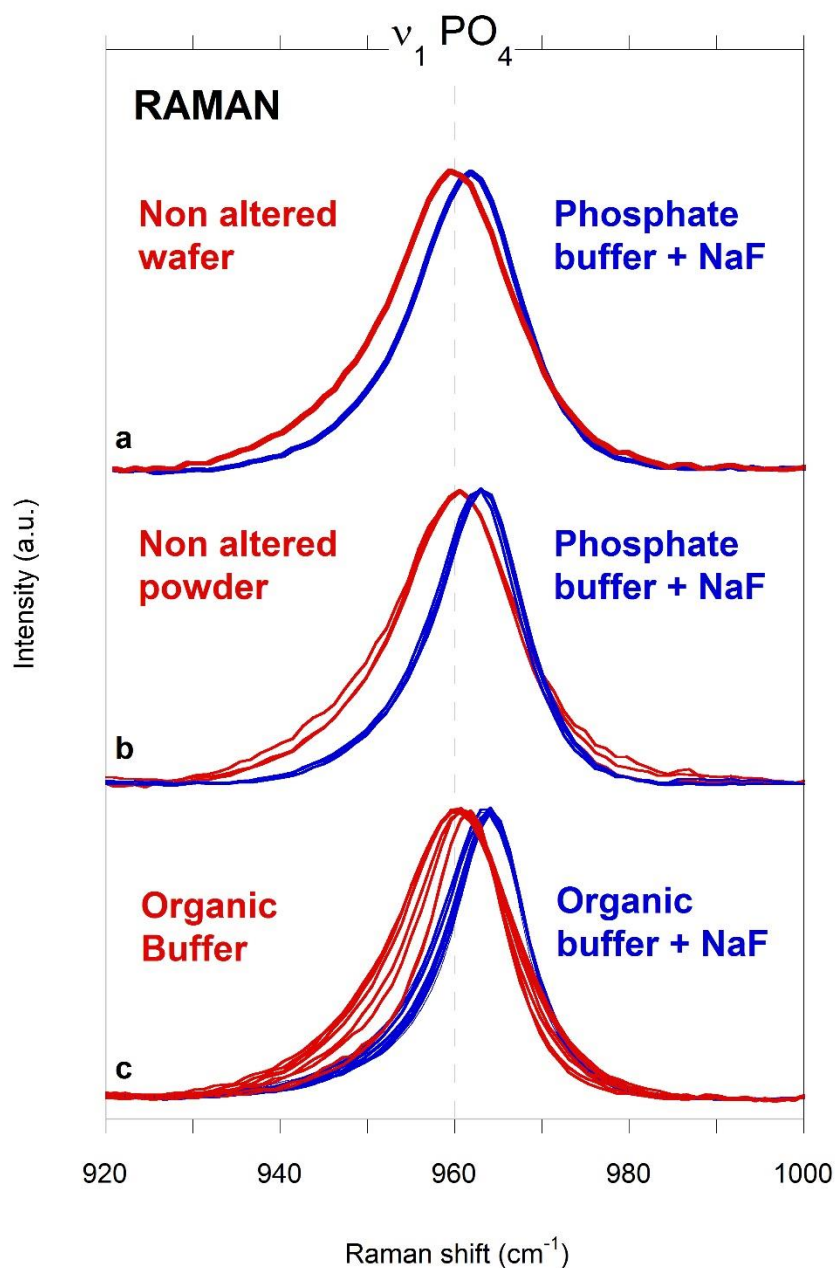
Figure 3 ν_1 PO$_4$ Ge ATR-FTIR bands (black line) of non-fluorinated and fluorinated bone samples in different buffers and pH conditions (Experiments C, D, E, F, G) compared to the unaltered bone material (TH1) and to sedimentary carbonated fluorapatite. Fits (red line) of the ν_1 PO$_4$ band in altered bones Ge ATR-FTIR spectra were achieved using two components: a Gaussian signal whose position and width was kept fixed to that of the unaltered bone TH1 (orange line) and a Lorentzian signal whose position was kept fixed in fluorinated samples and free in non-fluorinated samples (green line). Parameters of the fits are reported in Table 6. Percentages of the second component are indicated on the right-hand side of the figure.
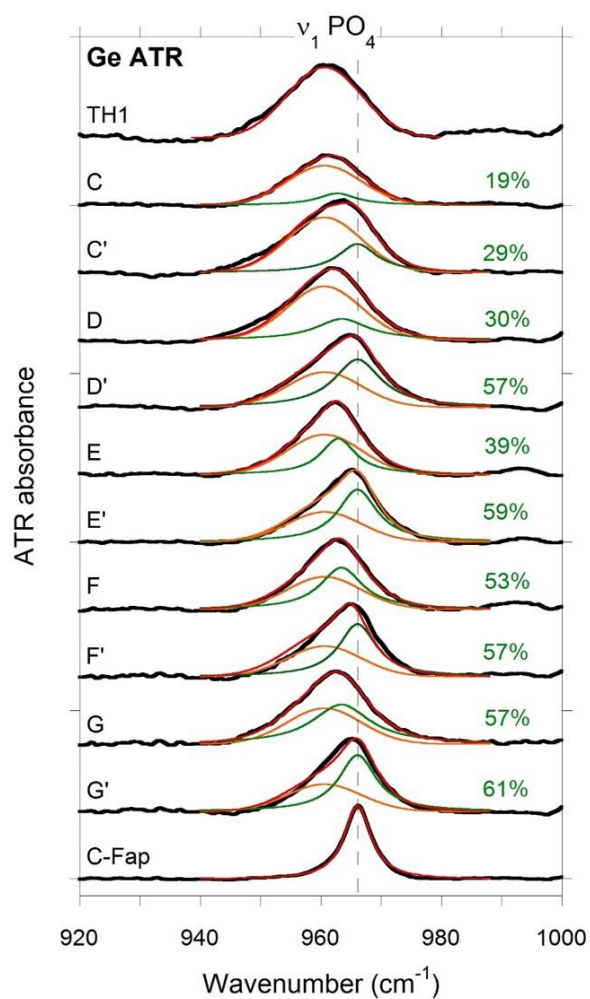
Figure 4 a. Raman spectra of the ν_1 PO_4 band in unaltered bone wafer and in bone wafer altered with 10^{-2} M NaF in a phosphate buffer solution for 1 weeks at 20°C (Experiment A). **b.** Raman spectra of the ν_1 PO_4 band in unaltered bone powder and in bone powder altered with 10^{-2} M NaF in a phosphate buffer solution for 3 weeks at 20°C (Experiment C). **c.** Raman spectra of the ν_1 PO_4 band collected at various loci on a transect of bone wafer altered with and without 10^{-2} M NaF in an organic buffer solution for 3 weeks at 70°C (Experiment H). The vertical dashed line is guide for the eye.

Figure 5 a. ν_2 CO$_3$ diamond ATR-FTIR bands of non-fluorinated and fluorinated bone samples in different buffers and pH conditions (Experiments C, D, E, F, G) compared to unaltered bone TH1 and sedimentary carbonated fluorapatite C-Fap. All spectra are normalised based on the ν_4 PO$_4$ band intensity. **b.** ν_2CO$_3$ diamond ATR-FTIR band ascribed to the clumped defect in E', F' and G', obtained by subtracting the ν_2CO$_3$ band of the non-fluorinated sample from the ν_2CO$_3$ band of the fluorinated sample diamond ATR-FTIR spectra compared to the ν_2CO$_3$ band of carbonated fluorapatite. Peak areas are 0.09, 0.13 and 0.16 respectively. Subtracted spectra were normalised on the A and B components of the ν_2 CO$_3$ band.
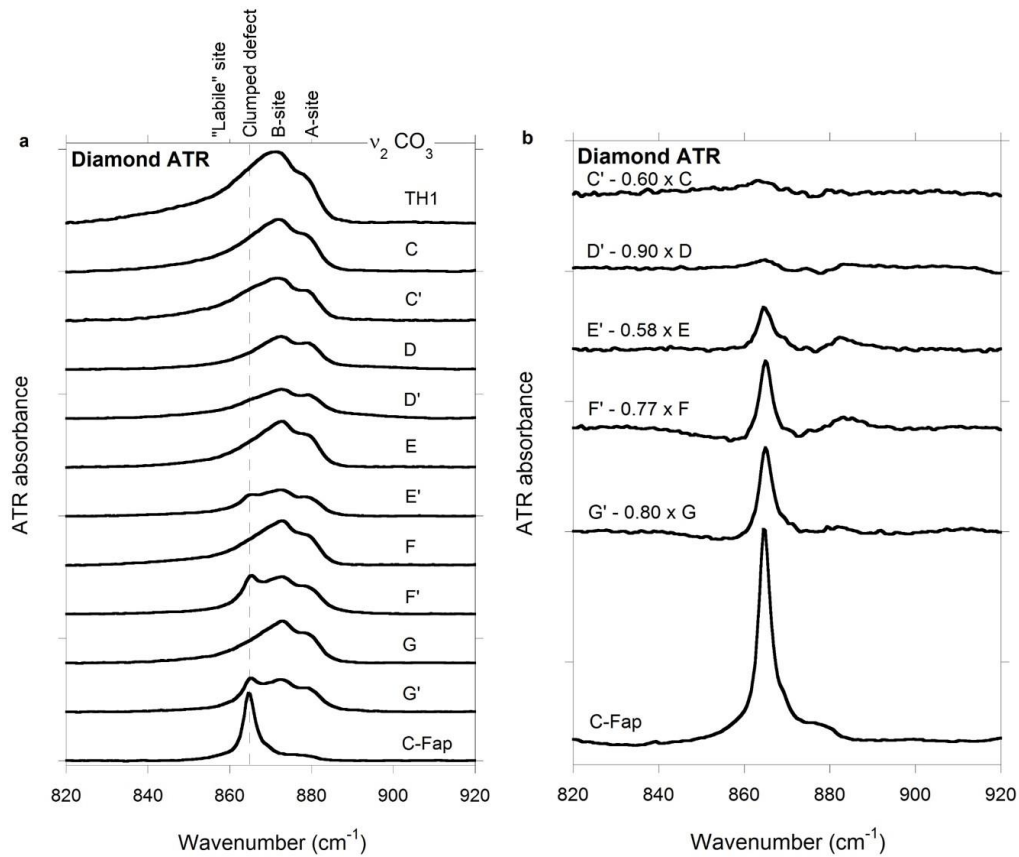
Figure 6 a. ^{13}C CP MAS NMR spectra of the unaltered bone, bones artificially altered with and without fluoride and ^{13}C MAS NMR spectrum of sedimentary carbonated fluorapatite. Signals comprised between 10 and 80 ppm correspond to organic carbon from the collagen matrix. **b.** Enlargement of the 140-200 ppm region of the ^{13}C CP MAS NMR spectra. Vertical dashed lines indicate the ^{13}C NMR positions of A-site and B-site carbonate signals. The component at ~173-175 ppm relates to the carboxylic acids from amino acids in the organic matrix. A vertical arrow is used to show the decrease in the latter component in the bone samples exhibiting a significant decrease in the organic fraction.
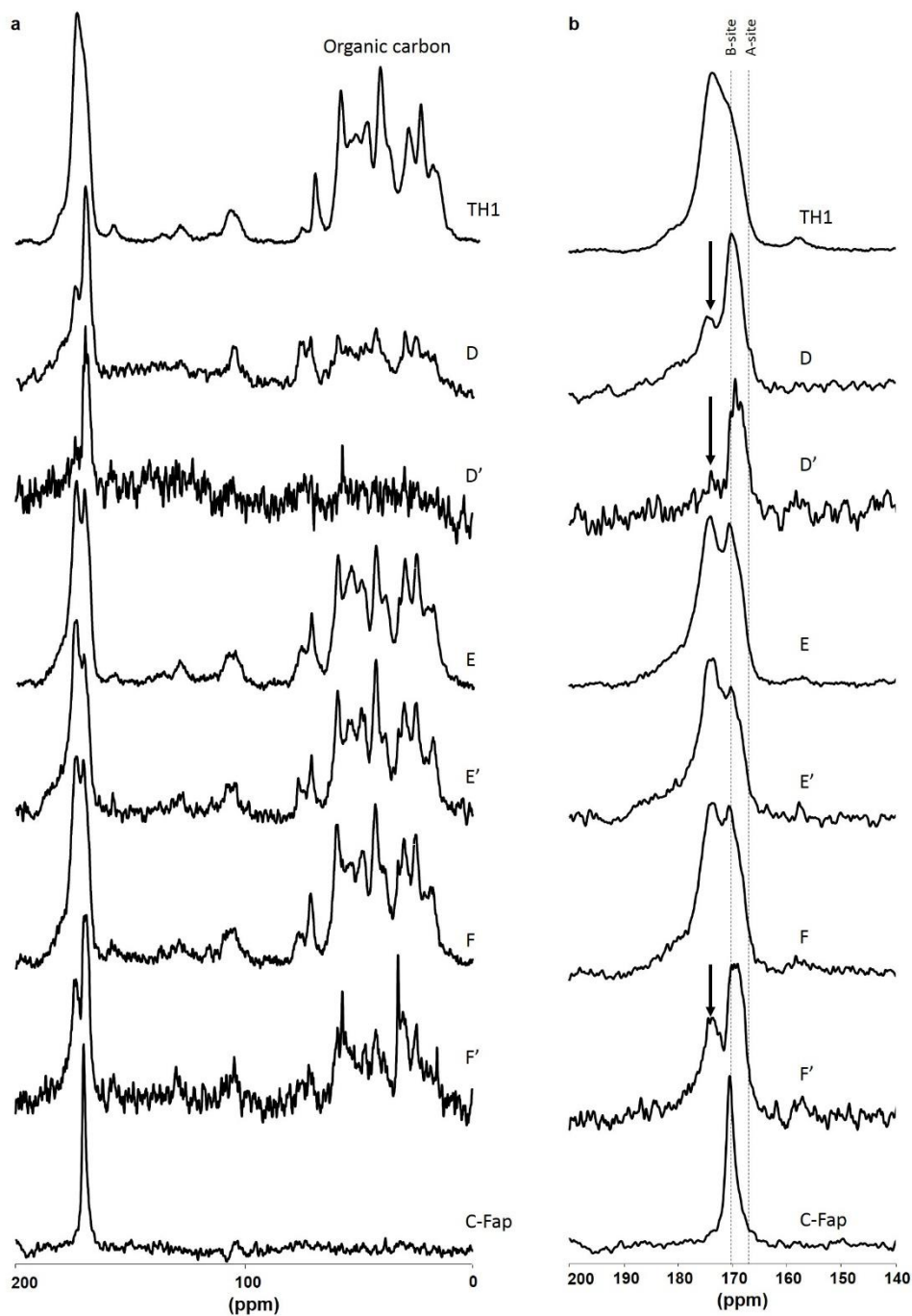
Figure 7 ^{19}F MAS NMR spectra of the bone samples altered with fluorine and sedimentary carbonated fluorapatite. Spectra are centred on the isotropic signal of the fluoride ions incorporated in the channels at -102 ppm with two spinning side bands on each side. The ^{19}F position of the clumped defect is indicated by a vertical dashed line.
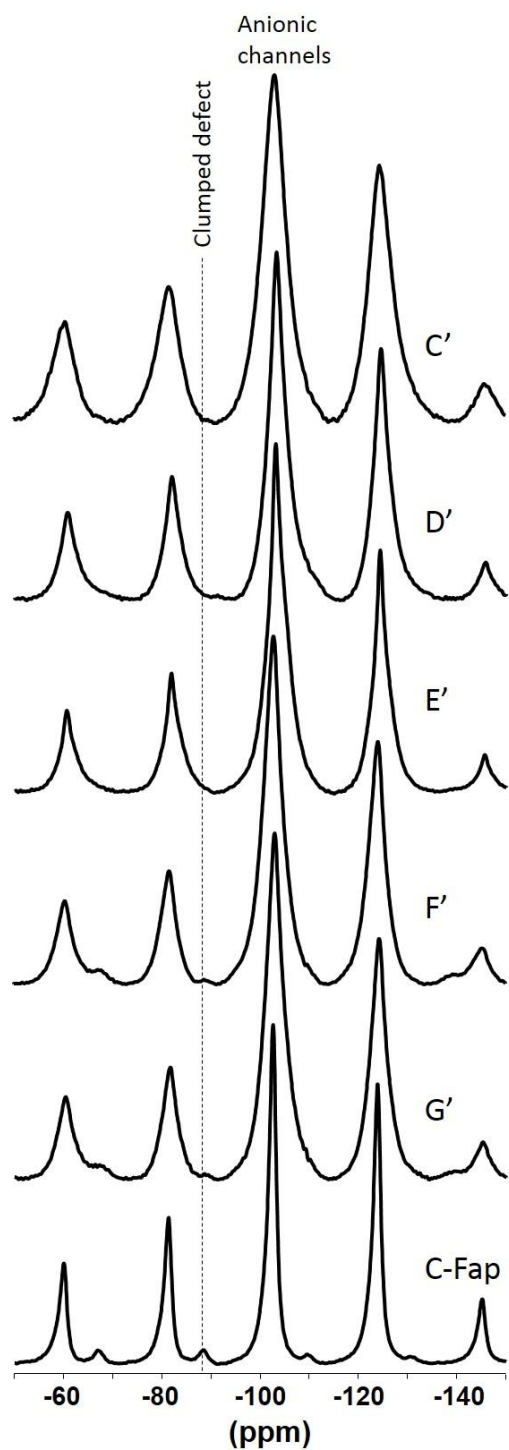
Figure 8 Evolution of (a) fluoride content, (b) ν_1 PO$_4$ Ge ATR-FTIR band frequency, (c) $\delta^{18}O_{carbonate}$ and (d) $\delta^{13}C$ as a function of the percentage of secondary apatite. Dashed lines are guide for the eye.
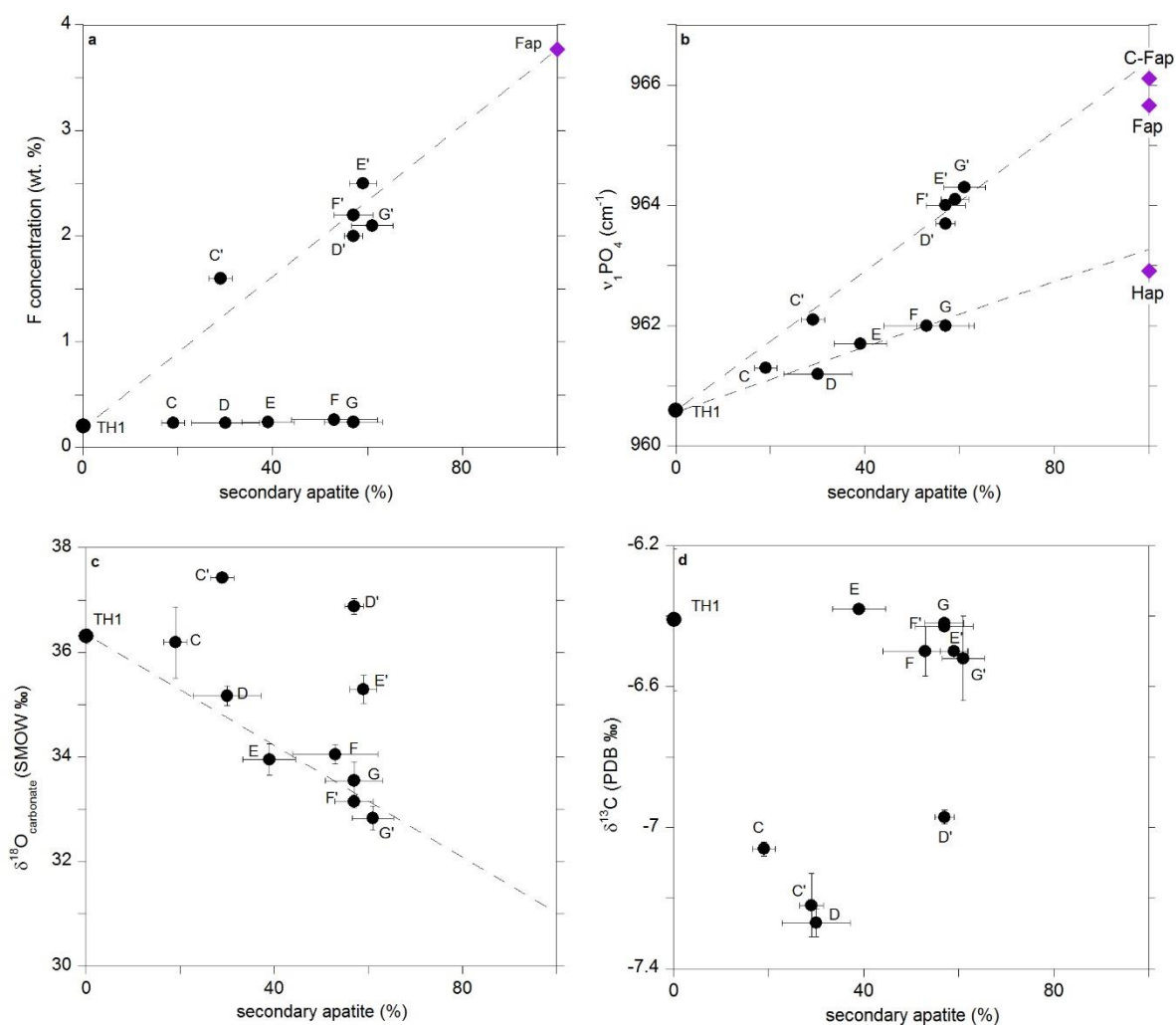
Figure 9 Comparison of ATR-FTIR Ge and Raman ν_1 PO$_4$ band position (a), FWHM (b) and asymmetry parameters (c).
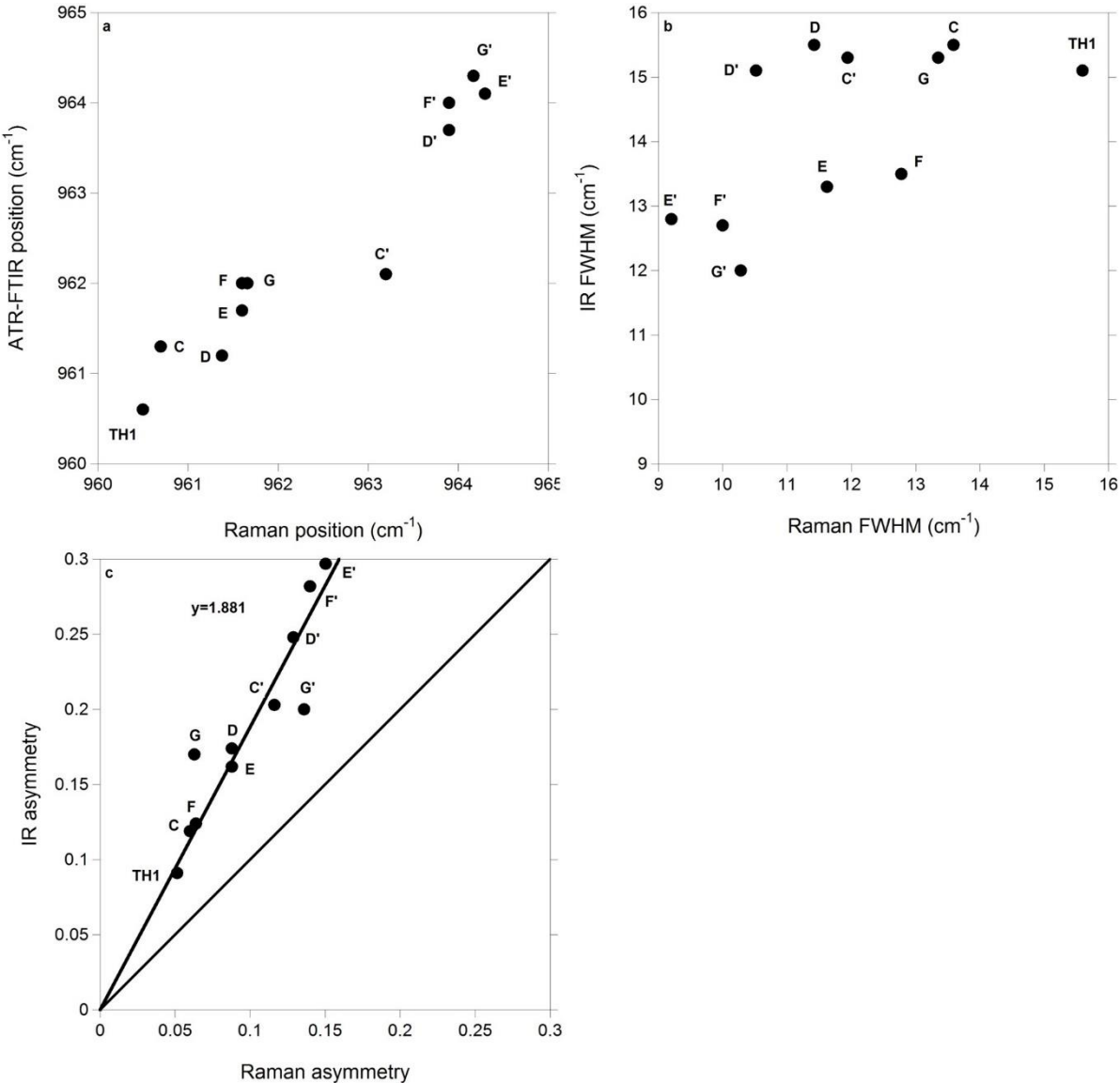
Figure 10 Hypothetical schematic representation of bone crystallites before and after dissolution-recrystallisation in the presence or absence of fluoride in the alteration solution. For a 4 x 20 x 30 nm^3 crystallite size, a maximum fraction of secondary carbonated apatite of 60 % corresponds to a ~1 nm thick layer. It is proposed that partial dissolution-recrystallization of bone occurs at the nanometre scale at the surface of each individual crystallite to account for the apparent maximal fraction of secondary phase and the lack of increase in MCD size. Note that the representation is not to scale.